Water-in-salt environment reduces the overpotential for reduction of CO_2 to CO_2^- in ionic liquid/water mixtures

Xiao-Hui Yang[a], Marco Papasizza[b,†], Angel Cuesta[b,c,] and Jun Cheng[a,d,*]*

[a] *State Key Laboratory of Physical Chemistry of Solid Surfaces, iChEM, College of Chemistry and Chemical Engineering, Xiamen University, Xiamen 361005, China.*

[b] *Department of Chemistry, School of Natural and Computing Sciences, University of Aberdeen, AB24 3UE, Scotland, UK.*

[c] *Centre for Energy Transition, University of Aberdeen, AB24 3FX, Scotland, UK.*

[d] *Innovation Laboratory for Sciences and Technologies of Energy Materials of Fujian Province (IKKEM), Xiamen, China.*

† Current address: Sweetch Energy, 6 Rue Pierre Joseph Colin, 3500 Rennes, France.

KEYWORDS: electrochemical reduction of CO_2, room temperature ionic liquid, *ab initio* molecular dynamics, absorption infrared spectra, hydrogen bond networks

ABSTRACT: We report a combined computational and experimental work aimed at estimating the equilibrium potential for the electroreduction of CO_2 to CO_2^- (widely accepted to be the first and overpotential-determining step) and at throwing new light on the reason behind the lower overpotentials for CO_2 reduction in imidazolium-based ionic liquid/water mixtures. First, we obtained an eighty-picosecond ab-initio molecular dynamics trajectory of the CO_2^- solvation structures in an 18% EMIM-BF_4/water mixture, which delivered no evidence of interaction between $EMIM^+$ and CO_2^-. Second, using the Fc^+/Fc couple as the non-aqueous reference, we calculated the equilibrium potential of the CO_2/CO_2^- couple in the mixture and aligned it with the aqueous SHE scale, proving that the equilibrium potential of CO_2/CO_2^- in the mixture is about 0.3 V less negative than in the aqueous medium. We then looked for the origin of this catalytic effect, by comparing the computed vibrational spectra with experimental FTIR spectra. This revealed the presence of two water populations in the mixture, namely, bulk-like water and water in the vicinity of EMIM-BF_4. Finally, we compared the hydrogen bonding interactions between the CO_2^- radical and H_2O molecules in water and in the mixture, which showed that stabilization of CO_2^- by water molecules in the EMIM-BF_4/water mixture is stronger than in the aqueous medium. This suggests that water in EMIM-BF_4/water mixtures could be responsible for the low overpotentials reported in this kind of electrolytes.

1. Introduction

The electrocatalytic reduction of CO_2 to hydrocarbons has great potential for large-scale applications. Recently, CO_2 electroreduction to CO at industrial-scale current density has been achieved,[1–4] which provides hope that the large-scale conversion of CO_2 to hydrocarbons using Cu cathodes is also feasible.[5,6] According to Weber's[7] approximate technoeconomic analysis,

there is a huge market for hydrocarbons and other commodity chemicals obtained from CO_2 electroreduction. However, this technology still faces challenges to become economically viable, one of the most important being the large overpotentials required.

According to our current understanding of the mechanism of CO_2 reduction to CO or HCOOH, the large energy difference between the linear CO_2 and the bent CO_2^- intermediate is the main responsible for the activation barrier.[8,9] Therefore, stabilizing CO_2^- would reduce the overpotential required for CO_2 electroreduction. Over the past decades, great success has been achieved in developing low overpotential electrochemical cells for electrochemical conversion of CO_2 to CO. Among the most outstanding is the system reported by Rosen *et al.*[10] in 2011, which employs an EMIM-BF_4/H_2O mixture (EBH mixture) as electrolyte and exhibits a claimed total overpotential of 0.17 V. Please note that this is the cell overpotential and should, therefore, be the sum of the anodic and cathodic overpotentials for oxygen evolution and CO_2 reduction, respectively, plus ohmic losses. As we have discussed in a recent review,[11] because oxygen evolution on Pt (the anode material used by Rosen *et al.*) in 0.1 M H_2SO_4 (the electrolyte in the anode compartment) alone requires an overpotential of at least 0.3-0.4 V, the reported overpotential of 0.17 V is impossibly low. The same group reported later a more reasonable onset cell overvoltage of 0.67 V,[12] which would correspond to a still remarkably low overpotential for the electroreduction of CO_2 to CO of *ca.* 0.3 V. Such low overpotential was attributed to the stabilization of the CO_2^- radical resulting from the first electron transfer in an EMIM-CO_2 complex.[10] However, this explanation remains controversial ten years after it was first proposed,[11,13–24] because there is still no evidence for the explanation provided by Rosen *et al.*, no matter how sophisticated the control experiments or complex theoretical calculations attempted.

In experiment, the CO_2^- radical was first detected during, and therefore confirmed as a key intermediate in, the electrocatalytic reduction of CO_2 by Bewick and co-workers[25] in 1973. This was later confirmed by others,[26] and the equilibrium potential of the CO_2/CO_2^- couple was determined in 1989.[27,28] Not much has been done since in terms of detection of the CO_2^- radical and characterization of its thermodynamic and kinetic properties, mainly due to its instability in water, which often forces experiments in solvents of low proton availability.[29]

Computational methods allow to study reactions involving unstable radicals[19,30–35] like CO_2^- without having to design sophisticated experiments. Another advantage of computational methods is that the reaction environment can be fully controlled, and quantifying the contribution of each component becomes feasible.[36] However, calculations of equilibrium potentials of redox couples (such as CO_2/CO_2^-) in non-aqueous solutions are difficult, even more in mixtures like EMIM-BF_4/H_2O solutions. Conventional implicit solvation models[37–43] face challenges in describing the charged solute (for example, the CO_2^- radical) in non-aqueous mixtures because of strong electrostatic interactions at the boundary between the solute and the implicit solvent. Even if explicit solvent molecules are included in the vicinity of the solute to compensate for the electrostatic effects, the calculation of cavitation energies is still questionable, not to mention the accuracy of parameterizations in describing the mixture solution. Therefore, there is a need to study CO_2 reduction in an explicitly described, consistent chemical environment as a prerequisite to completely understanding the electrocatalytic reduction of CO_2.

Ab initio molecular dynamics (AIMD) can explicitly describe both solutes and solvents at the same level of electronic structure theory, and thus the chemical environment is naturally consistent with experiments. By combining AIMD with free energy perturbation (FEP) methods, Cheng, Sprik and co-workers[30,44] have developed a thermodynamic scheme that can calculate

equilibrium potentials of any redox couples in any solution with respect to the computational SHE (in water) or Ag/AgCl (in non-aqueous solution)[45]. As a remarkable low overpotential for the CO_2 electroreduction was reported by Rosen *et al.*[10,12] in an 18 mol% EBH mixture, a rational option is to study the same electrolyte used in those works. Therefore, by using this method, we can calculate the CO_2/CO_2^- equilibrium potential in that EBH mixture. To quantify the decrease in overpotential in the EBH mixture, we need to compare the CO_2/CO_2^- equilibrium potential in the EBH mixture with that in water in the same potential reference scale. Since the equilibrium potential of ferrocenium/ferrocene (Fc^+/Fc) in 18 mol% EBH mixture with respect to SHE in water has been reported,[10] we can calculate the CO_2/CO_2^- equilibrium potential with respect to the Fc^+/Fc reference in the EBH mixture, and then align it with the SHE scale in water.[10,46] By using this approach, we can directly compare the equilibrium potentials of CO_2/CO_2^- in aqueous medium with that in the 18 mol% EBH mixture.

In this work, we combined computation and experiment to study the reduction of CO_2 to CO_2^- in the EBH mixture. First, we performed AIMD of both CO_2^- and CO_2 in the 18 mol% EBH mixture, investigating their solvation structures and exploring the existence of EMIM-CO_2 or -CO_2^- complexes. Then, we calculated the equilibrium potentials of the CO_2/CO_2^- and Fc^+/Fc redox couples with respect to the computational Ag/AgCl ($a_{Cl^-} = 1$) reference electrode (cAgCl) in the EBH mixture. As the experimental equilibrium potential of Fc^+/Fc against the Ag/AgCl electrode in ionic liquids has been reported, we were able to verify our computational results. Next, we aligned the CO_2/CO_2^- equilibrium potential in the 18 mol% EBH mixture with the SHE in water and compared with the CO_2/CO_2^- equilibrium potential in pure water, which revealed a clearly less negative equilibrium potential in the EBH mixture. Because the overpotential for the reduction of CO_2 is mainly attributed to the thermodynamic overpotential required to generate

the CO_2^-, this difference must result in a clearly lower overpotential in the EBH mixture. Finally, we compared computational vibrational frequencies of all the electrolyte media used in the AIMD study with experimental FTIR spectra, which allowed us to conclude that the hydrogen bond interactions between water molecules and CO_2^- in the EBH mixture are stronger than in the aqueous medium. The strong hydrogen bond interactions help stabilize the CO_2^- radical and thus reduce the overpotential required for CO_2 electroreduction.

2. Method

2.1 Computational methods

The method for the calculation of equilibrium potentials has been described in detail in previous publications.[30,44,45,47]. In this work, the equilibrium potentials were initially calculated against the cAgCl. For the convenience of the reader, we summarize below a few key points. The detailed derivation process can be found in the Supporting Information.

The free energy changes for the electron transfer or particle solvation reactions are calculated with a combination of the free energy perturbation (FEP) theory and the thermodynamic integration (TI) method. In this method, a thermodynamic path (η from 0 to 1) between two states is connected by a linear combination through a coupling parameter, where the two ends of the path ($\eta = 0$ and 1) correspond to the initial and final states, respectively. Thus, the free energy change (ΔA) is obtained using the TI method,

$$\Delta A = \int_0^1 d\eta \langle \Delta E \rangle_\eta, \quad (1)$$

where $\langle \Delta E \rangle_\eta$ is the ensemble average of the potential energy difference between the initial (E_0) and final (E_1) states at a fixed configuration ($\Delta E = E_1 - E_0$).[44]

Using the TI method in Eq. 1, the free energy of oxidation (reduction) from X^- to X (X to X^-) can be obtained by reversibly removing (inserting) an electron from the AIMD simulation under periodic boundary conditions (PBC). However, directly inserting an electron in a PBC system charges the system, and renders the reference for the electrostatic potential uncertain.[30] A computational Ag/AgCl ($a_{Cl^-} = 1$) reference electrode (cAgCl) is developed to recover the potential reference under PBC and align it to the experimental Ag/AgCl ($a_{Cl^-} = 1$) reference electrode.[45] For a specific oxidation reaction X^-/X with respect to the cAgCl, its full reaction is

$$X^-(aq) + AgCl(s) \longrightarrow X(aq) + Cl^-(aq) + Ag(s), \quad (2)$$

and the corresponding equilibrium potential ($U_{X^-/X}^{Ag/AgCl}$) can be obtained by

$$U_{X^-/X}^{Ag/AgCl} = (\Delta A_{X^-/X} + \Delta_f G_{Cl^-}^{g,o} - \Delta A_{Cl^-} + \Delta A_{LJ} - \Delta E_{Cl^-})/e_0. \quad (3)$$

Where $\Delta A_{X^-/X}$, ΔA_{Cl^-}, and ΔA_{LJ} are oxidation free energy of X^-/X, desolvation free energy, and formation energy of the Lennard-Jones cavity, respectively. All free energies (ΔA) in this work are obtained by using the Eq. 1. The $\Delta_f G_{Cl^-}^{g,o} = -1.3eV$ is the standard Gibbs free energy of formation of the gas phase chloride anion, and ΔE_{Cl^-} is the total energy of Cl^- in the gas phase. [45]

2.2 Modelling setup

In this work, we performed three AIMD simulations. To investigate the solvation structure of CO_2^- and calculate the $\Delta A_{CO_2^-/CO_2}$ for the equilibrium potential calculation, the CO_2/CO_2^- model in 18 mol% EBH mixture is conducted (Figure 1a). We also simulated the Fc/Fc^+ model (Figure 1b) and the Cl^- solvation model (Figure 1c) in 18 mol% EBH mixture to compute the equilibrium potential of Fc/Fc^+ with respect to cAgCl. Additionally, the equilibrium potentials of CO_2/CO_2^-

and Fc/Fc^+ with respect to cAgCl in a dilute aqueous solution (hereafter referred to as aqueous medium) were also calculated. For the reader's convenience, we summarise the key parameters of the calculations below. Details can be found in the Supporting Information.

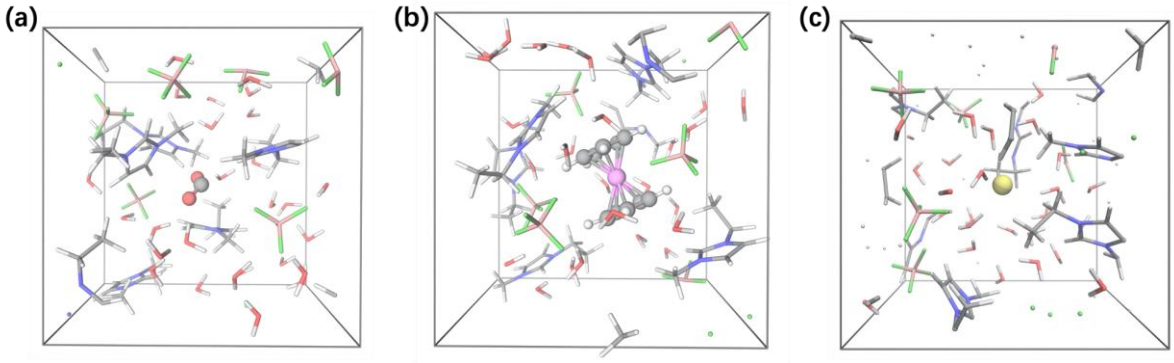

Figure 1. Snapshots of the simulations with solvated CO_2^- (a), ferrocenium (b), and chloride (c) in the 18 mol% EMIM-BF_4/H_2O mixture. Solutes are displayed using the ball-and-stick model, while the liquorice model presents the electrolyte molecules. Atoms are color coded as follows: purple is Fe, grey is C, red is O, yellow is Cl, white is H, blue is N, pink is B, and green is F. The electrolyte consists of 6 EMIM-BF_4 ion-pairs and 26 water molecules.

All AIMD simulations were performed with the open-source CP2K program. The density functional implementation in the CP2K/Quickstep[48] section is based on the hybrid Gaussian plane wave (GPW) scheme. In this work, we employed the BLYP functional[49,50], the Goedecker-Teter-Hutter (GTH) pseudopotentials[51,52] (core electrons in each element can be found in Table S2), TZP2P-GTH (models of CO_2/CO_2^- and Cl^- solvation) and DZVP-GTH (Fc/Fc^+ model) basis sets, and 400 Ry of the plane wave density cut-off. The dispersion correction was also applied in all calculations using the Grimme D3 method.[53] The free energy differences ΔA were recomputed at the hybrid functional level of theory (HSE06) using the trajectories generated by BLYP functionals, leading to an effective hybrid level of accuracy in the equilibrium potentials.

The simulation boxes are cubic cells with L = 13.39 (models of CO_2/CO_2^- and Cl^- solvation) and 13.8 Å (Fc/Fc^+ model). All boxes include 6 EMIM-BF_4 ion-pairs and 26 water molecules, plus 1 reactant molecule (e.g., CO_2^-, Cl^- or Fc^+) corresponding to the ambient density. The canonical (NVT) ensemble underwent Langevin molecular dynamics in this work and the temperature of the system was 300 K. To accelerate AIMD simulations, One of the AIMD families, the second-generation Car-Parrinello based molecular dynamics (SGCPMD) was used to sample configurations.[54] SGCPMD performs almost identical dynamics when compared with Born-Oppenheimer molecular dynamics (BOMD) but at a smaller computational cost.[55] Furthermore, in the CO_2/CO_2^- model, we replaced all the hydrogen atoms in this simulation with deuterium atoms and set the time step to 1 fs. The production runs of the SGCPMD simulations were about 80 ps after more than 10 ps equilibration. To validate the electronic structures described by the SGCPMD simulation, a 20 ps conventional BOMD trajectory with time step τ=0.5 fs was also obtained. Based on the results of CO_2/CO_2^- simulation, the vertical energy difference was converged within 20 ps. Therefore, for the Fc/Fc^+ and Cl^- solvation simulations, a timestep of 0.5 fs was used, and the production period of SGCPMD was reduced to about 20 ps after 10 ps equilibration.

2.3 ATR-IR

Absorption infrared spectra were recorded using a Nicolet iS50R FT-IR spectrometer equipped with a liquid N_2-cooled mercury cadmium telluride (MCT) detector and a homemade attenuated total reflectance (ATR) accessory, using unpolarized light. Differential spectra are reported in absorbance units and calculated as $-\log\left(\frac{R_{\text{sample}}}{R_{\text{reference}}}\right)$, where $R_{\text{reference}}$ and R_{sample} are the background and sample spectra, respectively. ATR absorption infrared spectra of EBH mixtures

were recorded by simply covering the surface of a Si prism with a liquid film of the mixture, using the spectrum of the dry Si prism as background. Both the background and sample spectra consisted of 100 interferograms with a spectral resolution of 4 cm^{-1}.

3. Results and discussion

3.1 CO_2^- solvation structures

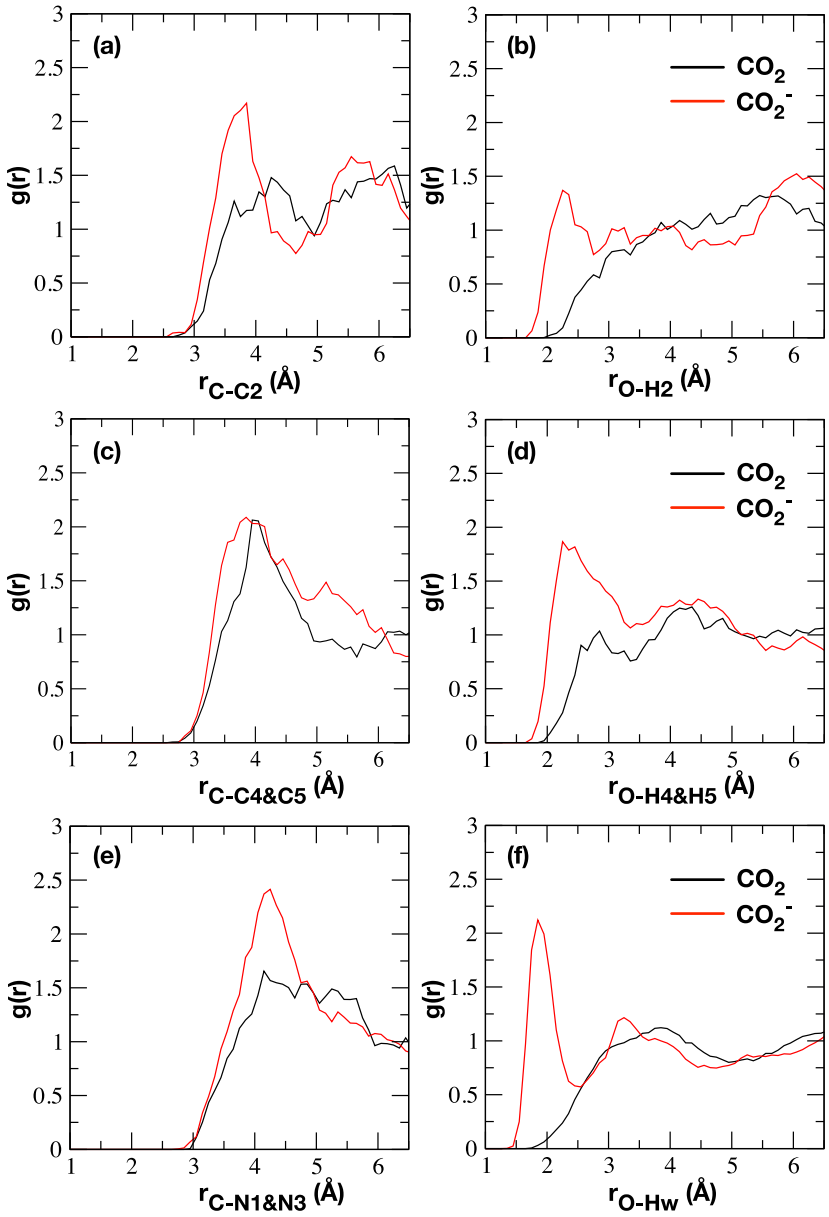

Figure 2. Comparison of solute-electrolyte radial distribution functions (RDF) for CO_2 (black line) and CO_2^- (red line) in 18 mol% EMIM-BF_4/water mixture. Graphs on the left show the distance between the C atom in CO_2 or CO_2^- and the C2 (a), C4&C5 (c), N1&N3 (e) sites of $EMIM^+$, while graphs on the right side illustrate hydrogen bonding interactions between O atoms in CO_2 or CO_2^- and H2 (b) and H4&H5 (d). The radial distribution function between O atoms in CO_2 or CO_2^- and H atoms in water (Hw) is shown in (f). The bin size for the evaluation of the distribution function is of 0.1 Å.

The CO_2^- radical complexation has been proposed as the possible reason behind lower overpotentials for CO_2 reduction in EMIM-BF_4. Therefore, we carefully investigated the solvation of both CO_2^- and CO_2 in the 18 mol% EBH mixture. After 80 ps AIMD simulation and 20 ps BOMD simulation, we found no evidence of interaction between CO_2^- and $EMIM^+$, *i.e.*, $EMIM^+$-CO_2^- complexes involving stable chemical bonds are not formed. However, this does not exclude the stabilization of CO_2^- through hydrogen bonding interactions and other electrostatic interactions. Figure 2 shows radial distribution functions (RDF) in the mixture solvent between C and O atoms of both CO_2^- and CO_2 and all the possible active sites on $EMIM^+$ (namely, C2/H2, C4/H4 and C5/H5, See Support Information for notations) as well as hydrogen atoms in water. Nitrogen atoms (N1 and N3) in $EMIM^+$ were also included in order to investigate the distance between CO_2^- or CO_2 and the $EMIM^+$ imidazole ring. According to Figures 2(a), (c) and (e), reduction of CO_2 to CO_2^- results in an increase of the coordination number of $EMIM^+$ around the solute, while the distance between $EMIM^+$ and the C atom of the solute remains constant. This implies that there is no specific interaction between the C atom of CO_2^- and $EMIM^+$, as the increase of the coordination number can simply be explained by the electrostatic attraction between CO_2^- and $EMIM^+$. In contrast, Figures. 2(b) and (d), show that reduction of CO_2 to CO_2^-

results in a decrease of the distance between the oxygen atoms and the H4/H5 sites, which seems in agreement with Lau *et al.*'s[13] conclusion that H4 and H5 help stabilize the CO_2^- radical. However, the maximum lies at $r_{O\text{-}H4\&H5}$ = 2.5 Å, indicating that there is no interaction between them. Interestingly, the maximum at $r_{O\text{-}Hw}$ = 1.8 Å, characteristic of hydrogen bonding, appearing in Fig. 2(f) upon reduction of CO_2 to CO_2^- implies that water molecules in the mixed solvent must play an important role in stabilizing the radical. An intuitive view of the interactions between water molecules and CO_2^- is presented in Figure 3(a).

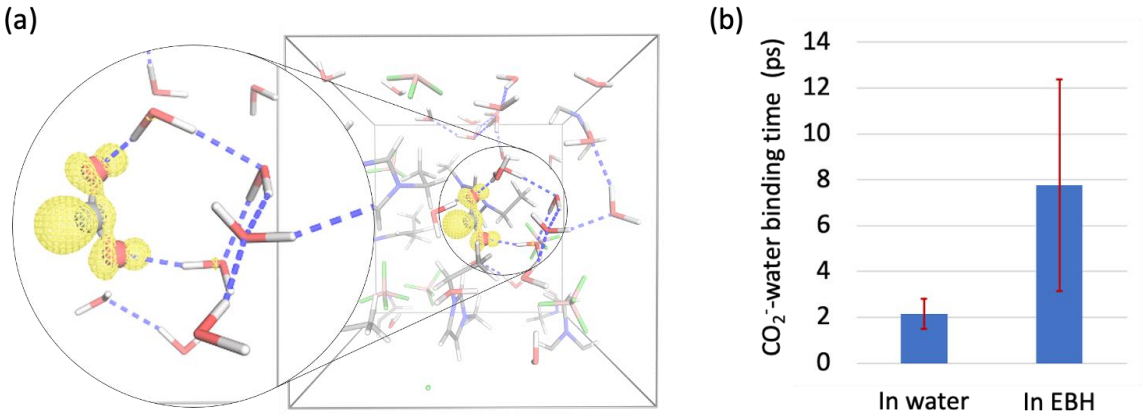

Figure 3. (a): A snapshot of CO_2^- solvation structure in the EMIM-BF_4/water mixture. The yellow region is the excess electron density in the CO_2^- model. The figure inside the left circle is the enlarged view of the central region close to CO_2^-, and the blue dashed lines are hydrogen bonds formed in this snapshot. A few molecules have been removed in the enlarged figure for a clear view of the hydrogen bond networks between CO_2^- and electrolyte molecules. (b): CO_2^--water binding times obtained from AIMD trajectories in water and in EBH.

Figure 3(a) suggests the formation of hydrogen bonds between CO_2^- and water molecules in the EBH mixture. In principle, it might seem that a similar situation would arise in aqueous solutions. In fact, our simulations reveal that the total number of hydrogen bonds around the

solute is the same in pure water and the EBH mixture. Nevertheless, based on the simulation trajectories, in the EBH mixture CO_2^- forms stable hydrogen bonds with specific water molecules which do not exchange with other water molecules. In contrast, although hydrogen bonds were also formed in the aqueous medium, these do not correspond to specific water molecules interacting with CO_2^-, but are continuously being exchanged with other water molecules in the bulk. The CO_2^--water binding time obtained from trajectories in Figure 3(b) proved that the dynamics of water molecules in the EBH are about four times slower than in water. The consequence of these slow dynamics is that CO_2^- forms stable hydrogen bonds with specific water molecules which do not exchange with other water molecules.

3.2 Equilibrium potentials

Based on the solvation structure in Figure 3, a direct catalytic contribution of the EBH to CO_2 reduction is quite doubtful. A reduction in overpotential could, however, also stem from the observed change in solvation for EBH mixtures vs. aqueous environment discussed above. To compare the equilibrium potential of the CO_2/CO_2^- in EBH mixture with that in water, we need to compute both in~~at~~ the same reference potential scale. Using Eq. 3 and Eq. S14, we calculated the equilibrium potentials of CO_2/CO_2^- and Fc/Fc^+ redox couples in the 18 mol% EBH mixture with respect to cAgCl in different levels of density functional theory (DFT) approximation, and computed band edges of the electrolyte. Band edges of the electrolyte, which are the valence band maximum (VBM) and the conduction band minimum (CBM), can be calculated from the average energy of the highest occupied molecular orbital (HOMO) and lowest unoccupied molecular orbital (LUMO) of the mixture, respectively. Results of vertical energy gaps $\langle \Delta E \rangle_\eta$ and the corresponding thermodynamic integrations ΔA are presented in Figure 4(a), and all values required in Eq. 3 and Eq. S14 can be found in Tables S5-S8 in the Supporting

Information. In Figure 4(b), we summarize all equilibrium potentials and band-edge positions of the 18 mol% EBH mixture with respect to cAgCl under different DFT approximations. The CBM is 0.3 V more positive at the generalized gradient approximation (GGA) level of theory than with the hybrid functional HSE06, which also shifts the CO_2/CO_2^- and Fc^+/Fc equilibrium potentials positively by about 0.1 V. The VBM of the mixture is about 1 V more negative at the GGA level of theory than with hybrid functional HSE06, which is caused by the delocalization error of DFT at GGA level.

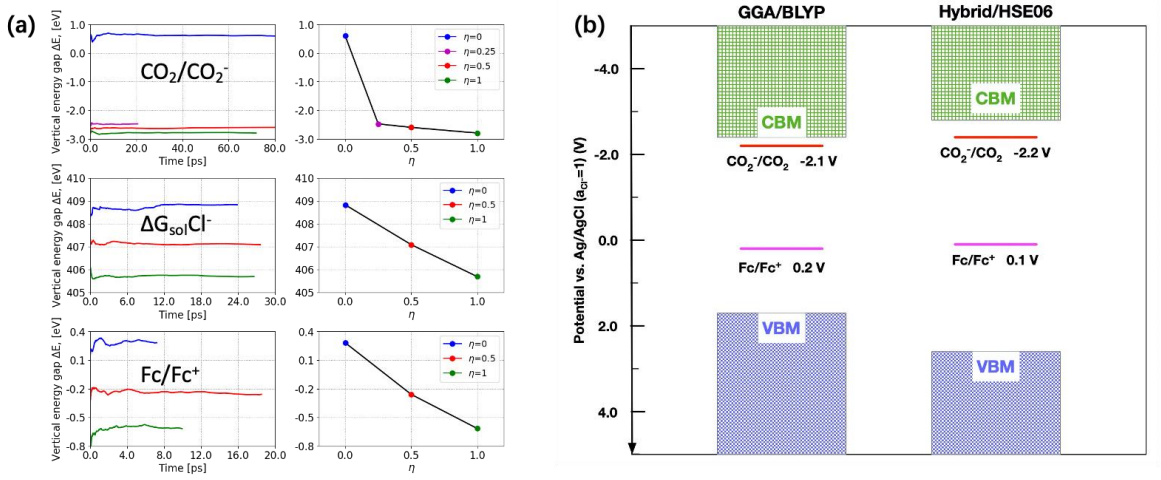

Figure 4. (a) Time accumulation averages of the vertical energies ($\langle \Delta E \rangle_\eta$, left column) and the corresponding thermodynamic integrations (ΔA, right column) obtained in this work. Three models from top to bottom are CO_2/CO_2^- model, Cl^- solvation model, and Fc^+/Fc model. (b) Equilibrium potentials of CO_2/CO_2^-, Fc^+/Fc and band-edge positions of the 18mol% EBH mixture with respect to the cAgCl under different DFT approximations. The GGA level BLYP functional is on the left, and the right is the hybrid level HSE06 functional.

We then calculated the equilibrium potentials of CO_2/CO_2^- and Fc/Fc^+ with respect to cAgCl in the aqueous medium, and report all equilibrium potentials in Table 1. Results obtained

in the aqueous medium can be directly compared with the experiment, and the error is about 0.1 V. This error is within our computational uncertainty, and thus implies that the DFT approximations made result in negligible errors in the computation of CO_2/CO_2^- and Fc/Fc^+ equilibrium potentials. However, verifying equilibrium potentials in the EBH mixture is a challenge, because (1) there are few experimental values of the equilibrium potential of Fc/Fc^+ in this EBH mixture, and (2) the reference electrode employed in those experiments cannot be directly compared to cAgCl. Nevertheless, we still attempted to roughly verify the equilibrium potentials in the EBH mixture, even if with a few approximations.

Table 1. Equilibrium potentials of the CO_2/CO_2^- and Fc/Fc^+ redox couples with respect to cAgCl in both aqueous medium and 18 mol% EBH mixture.

CO_2/CO_2^- vs. Fc/Fc^+	(unit in V)	
Aqueous medium	Exp.	-2.30[a]
Aqueous medium	Cal. (BLYP)	-2.40[b]
18 mol% EBH mixture	Cal. (BLYP)	-2.28
18 mol% EBH mixture	Cal. (HSE06)	-2.27
Fc/Fc^+ vs. cAgCl	(unit in V)	
Aqueous medium	Exp.	0.18[a]
Aqueous medium	Cal. (BLYP)	0.29[c]
18 mol% EBH mixture	Cal. (BLYP)	0.20
18 mol% EBH mixture	Cal. (HSE06)	0.11

[a]Experimental results adopted from CRC handbook.[56]

[b]The computational results of CO_2/CO_2^- in pure water were adopted from Cheng et al's work.[30]

[c]Computational details of Fc/Fc^+ equilibrium potential in pure water are provided in section S4 in the Supporting Information.

The equilibrium potential of the Fc/Fc^+ redox couple is often used as reference in several non-aqueous electrolytes (IUPAC recommendations). However, the stability of the Fc/Fc^+ redox couple fails in the presence of water, which prevents its use in aqueous solutions. Please note that the Fc/Fc^+ equilibrium potential has to depend on the solvent, as the (electro)chemical potential of the species involved in the electrochemical equilibrium will be different. For example: in aqueous solution, the Fc/Fc^+ equilibrium potential versus the aqueous SHE is 0.40 V,[56] while in non-aqueous electrolytes, a considerable higher equilibrium potential (*ca.* 0.65 V) with respect to the aqueous SHE has been reported.[46]

Rosen *et al*.[10] used an Ag/Ag^+ electrode immersed in CH_3CN (ANE) as their reference state. They reported the potential of the ANE in the 18 mol% EBH mixture to be 0.631 V against the aqueous SHE, and an Fc/Fc^+ equilibrium potential in the same EBH mixture of -5.5 mV with respect to ANE. This yields an Fc/Fc^+ equilibrium potential in 18 mol% EBH mixture of 0.625 V vs. aqueous SHE, which we use to convert the equilibrium potential of CO_2/CO_2^- in the EBH mixture to the aqueous SHE scale. We summarize the potential alignment result in Figure 5, where the scale on the left corresponds to the potential *vs.* Fc/Fc^+ in EBH. The scales on the right side of Figure 5 correspond to the aqueous SHE and cAgCl. By definition, the cAgCl is the same as the experimental AgCl reference electrode, and thus the alignment between cAgCl and SHE uses the experimental value of 0.222V vs. SHE (a_{Cl^-} = 1 in the definition of cAgCl). Please note that scales in different electrolytes cannot be aligned unless a reference state is measured on both scales. Fortunately, we know that the Fc/Fc^+ equilibrium potential in 18 mol% EBH mixture is 0.625 V with respect to the aqueous SHE scale. This allows to align the Fc/Fc^+ scale in EBH with the SHE scale in water in Figure 5. We can now locate the position of the CO_2/CO_2^-

equilibrium potential using Table 1. The equilibrium potential of CO_2/CO_2^- vs. Fc/Fc^+ is -2.27 V in the EBH mixture and is -2.40 V in water.

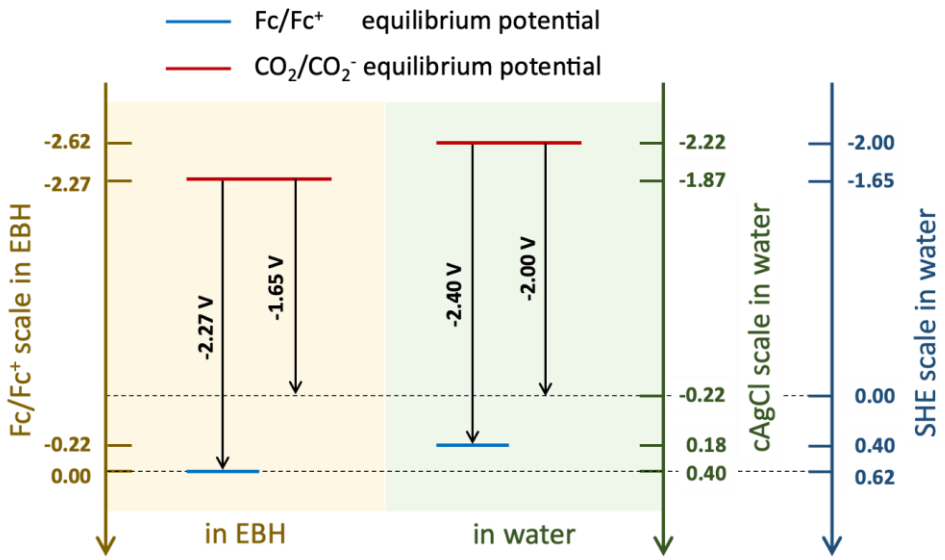

Figure 5. A schematic view of potential alignments between the Fc/Fc^+ reference state in 18 mol% EBH mixture and the aqueous SHE scale. The alignment between cAgCl and SHE uses the experimental value of 0.222V vs. SHE (a_{Cl^-} = 1 in the definition of cAgCl). The Fc/Fc^+ equilibrium potentials in 18 mol% EBH mixture is 0.625 V with respect to the aqueous SHE.[10]

If we refer the CO_2/CO_2^- equilibrium potential to the aqueous SHE scale, we obtain a value of -1.65 V in the EBH mixture (Figure 5), which is about 0.3 V lower than in water, in very good agreement with the experimental overpotential reduction reported by Rosen *et al.*[12] Please note that we use the computational result of the CO_2/CO_2^- equilibrium potential in water (-2.4 V in Table 1) instead of the experimental value (-2.3 V in Table 1), because the difference between two computational results should be more accurate due to error cancellations. Together with the result in Section 3.1 we can conclude that the stabilization of the CO_2^- radical by hydrogen bonding with water molecules in the 18 mol% EBH mixture, and not the formation of

EMIM-CO_2 complexes, is responsible for the reported decrease of the overpotential of CO_2 electroreduction of about 0.3 V.

3.3 Water in EBH mixtures

Please note that the conclusion above excludes any additional catalytic contribution from the electrode, and thus the only possible way to stabilize the CO_2^- radical in the EBH mixture is the hydrogen bond interaction between the oxygen of CO_2^- and the hydrogen of H_2O. In a recent spectroelectrochemical study of the electrocatalytic reduction of CO_2 to CO on Au electrodes in an 18 mol% EBH mixture, Papasizza and Cuesta[14] identified two water populations characterized by O-H stretching frequencies centred at 3610 and 3400 cm^{-1}, respectively. They identified these as water with a low degree of hydrogen bonding in an EMIM-BF_4-rich environment (3610 cm^{-1}) and bulk-like water (3400 cm^{-1}), and suggested that these two types of water might play different roles during the electrocatalytic reduction of CO_2. It is consistent with common sense that, in the EBH mixture, the large $EMIM^+$ and BF_4^- ions disrupt the hydrogen bond network and separate water molecules into isolated populations with different behaviour. This is also confirmed by our simulation trajectories.

Inspired by the snapshot in Figure 3, we took a closer look at the solvation structure around CO_2^- and identified five types of water in the EBH mixture as illustrated in Figure 6(a). Water molecules are separated based on their hydrogen bonding interactions with other molecules. In Figure 6(a), water #1 and water #5 both have a H atom interacting with an O atom in the CO_2^- radical, and we identify the corresponding O-H stretching mode in water as $\nu_{\mathrm{OH-OC}}$. In water #5, the other H atom interacts with the O atom in water #2. We identify the corresponding O-H stretching mode as $\nu_{\mathrm{OH-OH}}$. In contrast, the other H atom in water #1 hardly

interacts with other molecules and is therefore identified simply as ν_{OH}. Accordingly, the two O-H stretching modes in water #2 are both $\nu_{\mathrm{OH-OH}}$. In water #3, one of the H atoms interacts with a F atom in BF_4^-, and this O-H stretching mode is identified as $\nu_{\mathrm{OH-F}}$. Water #4 is water in an EMIM-BF_4-rich environment and has therefore none of its two hydrogen atoms is hydrogen bonded to any other atom. Both of its O-H stretching modes are identified as ν_{OH} in Figure 6(a).

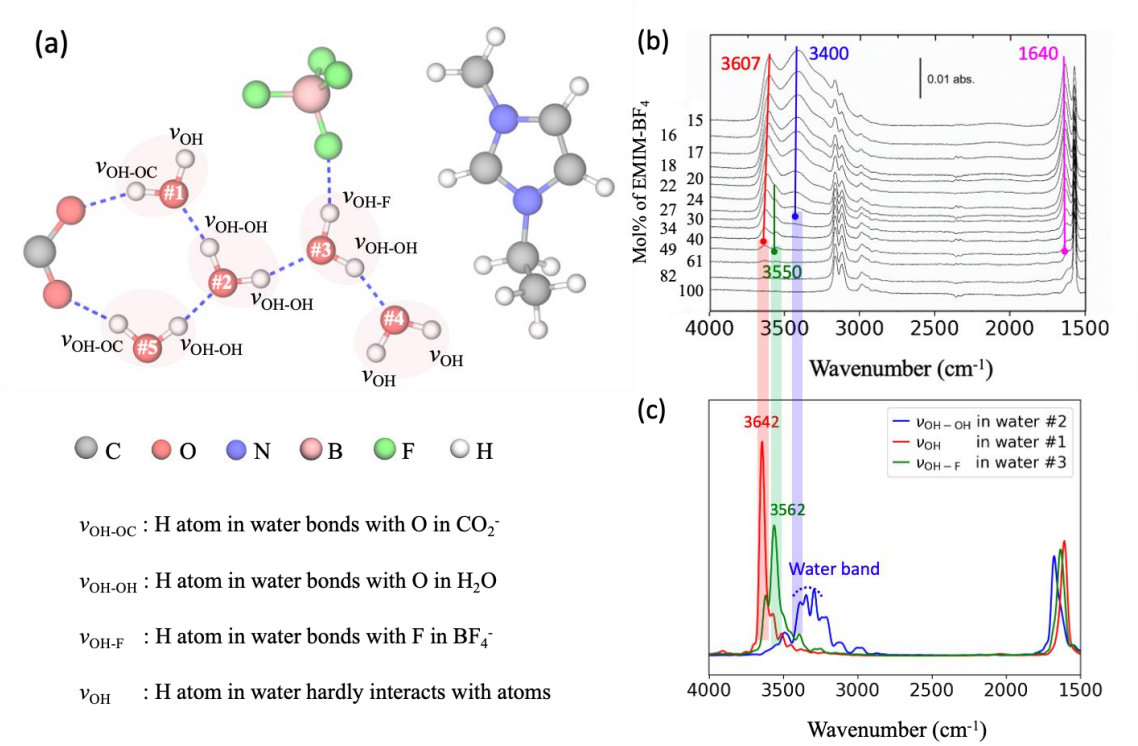

Figure 6. (a): An illustration of the CO_2^- solvation structure in the EBH mixture. Five types of water molecules are marked by #1 to #5. (b): Experimental ATR infrared absorption spectra of EMIM-BF_4/H_2O mixtures with increasing water content. The y-axis corresponds to the mol% of EMIM-BF_4. (c): Computed power spectra of the three possible O-H stretching modes ($\nu_{\mathrm{OH-OH}}$, $\nu_{\mathrm{OH-F}}$, and ν_{OH}) corresponding to the three possible different environments in 18 mol% EMIM-BF_4/water mixtures.

The ATR infrared absorption spectra of EBH mixtures with increasing concentration of water shown in Figure 6(b) confirm the correctness of the assignment in our previous work[14] of the bands at 3610 and 3400 cm^{-1} to water with a low degree of hydrogen bonding in an EMIM-BF_4-rich environment and bulk-like water, respectively. The peak at 3607 cm^{-1}, and a smaller one at ca. 3550 cm^{-1} which disappears for mixtures with less than 20% EMIM-BF_4, are absent in 100% EMIM-BF_4 and are the only bands present in the region characteristic of O-H stretching modes when the ionic liquid content is between 82 and 49%, confirming that this must correspond to water molecules in an EMIM-BF_4-rich environment with very few, if any, hydrogen bonds with other water molecules. The band at 3607 cm^{-1} in Figure 6(b) is consistent with the O-H stretching mode with a low degree of hydrogen bonding, *i.e.*, ν_{OH} in Figure 6(a). Since water #1 has this O-H stretching mode with a low degree of hydrogen bonding, we calculated its power spectrum by using the velocity autocorrelation function (VACF) method on top of AIMD trajectories, and present the result in Figure 6(c) (red line). The peak around the 3642 cm^{-1} indicates that our assignment is consistent with the experimental transmission spectra. As a verification, the experimental band at 3560 cm^{-1} is consistent with the $\nu_{\mathrm{OH-F}}$ stretching mode of water #3 computed at 3562 cm^{-1}, as is the experimental trend that this band only exists when the EMIM-BF_4 content is high. The typical bulk-water OH stretching band around 3400 cm^{-1}, with a shoulder around 3300 cm^{-1} which becomes clearer as water content increases, only appears with mixtures containing less than 40% ionic liquid. Its intensity increases with increasing water content. We attribute this band to bulk-like water with a structure and degree of hydrogen bonding similar to liquid water. The results are consistent with the spectrum of $\nu_{\mathrm{OH-OH}}$ in Figure 6(c). The band corresponding to the H-O-H bending mode of water appears at a lower frequency around 1610 cm^{-1} in the mixtures with low water content. Its frequency increases

towards 1640 cm^{-1} with increasing water concentration, which is also consistent with an increase in the degree of hydrogen bonding. Interestingly, in Figure 6(c), we found the same trend of the H-O-H bending mode from 1610 cm^{-1} to 1680 cm^{-1}. Please note that, although we have focused our discussion of the computational power spectrum on the O-H stretching modes (*e.g.*, ν_{OH} or ν_{OH-F}), the spectrum contains all the vibrational information in water, including the vibrational frequencies of the H-O-H bending mode, which are therefore also present in Figure 6(c). The computed vibrational frequencies of the H-O-H bending mode, from lower to higher degree of hydrogen bonding interactions, are 1609 $cm^{-1}(\nu_{OH})$, 1634 $cm^{-1}(\nu_{OH-F})$, and 1676 $cm^{-1}(\nu_{OH-OH})$, respectively.

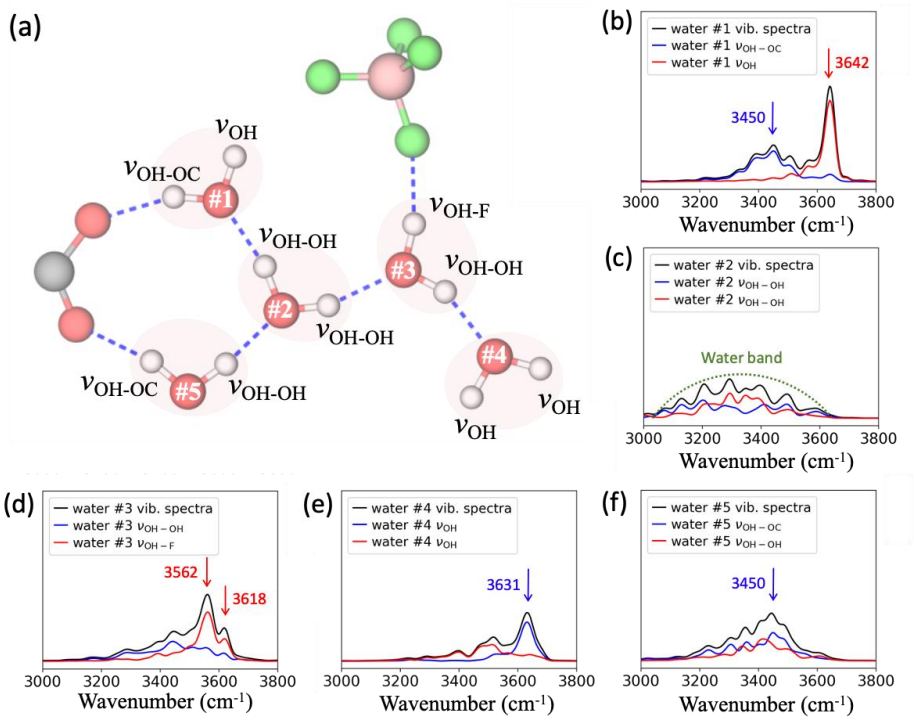

Figure 7. (a): An illustration of the CO_2^- solvation structure in the EBH mixture. Five types of water molecules are marked by #1 to #5. (b)-(f): Computed power spectra in the O-H stretching

region of water types #1 to #5 (black lines). The spectra corresponding to each one of the specific OH vibrations of water types #1 to #5 are illustrated with red and blue lines.

To study how the CO_2^- radical is stabilized by water molecules, we focus on the five types of water molecules in the EBH mixture described above, and calculated their corresponding power spectra in Figures 7(b)-(f). In each one of Figures 7(b) to (f), we include the total power spectrum of water (black lines) and the computed spectrum of each of the O-H stretching modes of each specific type of water (red and blue lines). Based on the results in Figures 7(b) and (f), the O-H stretching mode $\nu_{\mathrm{OH-OC}}$ due to the hydrogen bonding interaction between water #1 and #5 with the CO_2^- radical in the EBH mixture is 3450 cm^{-1}. The hydrogen bonding interaction between water and the BF_4^- anion is weaker, and thus the O-H stretching mode $\nu_{\mathrm{OH-F}}$ is 3562 cm^{-1}. The wavenumber of the O-H stretching mode is further increased if the H atom in water hardly interacts with other molecules, *i.e.*, has a low degree of hydrogen bonding interactions, and the corresponding value of ν_{OH} is higher than 3600 cm^{-1}. The spectrum of $\nu_{\mathrm{OH-F}}$ in Figure 7(d) shows two peaks at 3562 cm^{-1} and 3618 cm^{-1}, respectively. This is due to the occasional break of the hydrogen bond between the H atom in water #3 and the F atom in BF_4^-, leading to an increase in the wavenumber, which becomes similar to ν_{OH}.

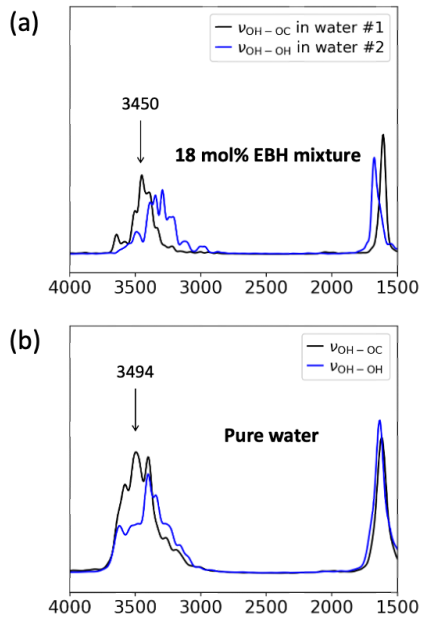

Figure 8. Computed power spectra of the ν_{OH-OC} (black lines) and ν_{OH-OH} (blue lines) modes in the 18 mol% EBH mixture (a) and in pure water (b) of CO_2^-.

We also calculated the power spectrum of an aqueous solution containing CO_2^- (Figure 8(b)), where ν_{OH-OH} and ν_{OH-OC} correspond to the same vibrational modes as in the EBH mixture (see Figure 6(a)). Comparing with the power spectrum of CO_2^- in EBH (Figure 8(a)), the ν_{OH-OC} blueshifts from 3450 cm^{-1} to 3494 cm^{-1} in pure water. Here, our computation captures the shift of the ν_{OH-OC} due to interaction with different electrolytes. The lower wavenumber of ν_{OH-OC} in EBH suggests that hydrogen bonding interactions between water molecules and the CO_2^- radical are stronger in the EBH mixture than in pure water. We believe that this enhanced hydrogen bonding between water molecules and the CO_2^- radical is responsible for the stabilization of CO_2^- in the EBH mixture, reducing the overpotential of CO_2 electroreduction by 0.3V.

4. Conclusions

Our work shows that the solvation structure of the CO_2^- radical in the EBH mixture does not reveal any interaction between CO_2^- and $EMIM^+$ that might account for a stabilization of the radical intermediate and, therefore, a decrease of the apparent activation energy. We found, however, stable hydrogen bonding with specific water molecules in the EBH mixture. In order to quantitively confirm whether the overpotential decrease in the EBH mixture can be attributed to the reduction of the potential required for electroreduction of CO_2 to CO_2^-, the equilibrium potential of this redox couple was calculated with respect to the Fc^+/Fc in the same electrolyte. We then converted the reference state from the Fc^+/Fc in EBH mixture to the aqueous SHE scale and found a positive shift of approximately 0.3 V of the CO_2/CO_2^- equilibrium potential in the EBH mixture as compared to the aqueous medium. Finally, we compared experimental and computed vibrational spectra of water in aqueous solution and in the EBH mixture, with CO_2^- present in both cases, which suggested that hydrogen bonding between water molecules and CO_2^- in in the EBH mixture is stronger than with water in the aqueous medium. This enhancement of the hydrogen bonding interactions renders the CO_2^- intermediate more stable in the EBH mixture, thus accounting for the overpotential decrease for CO_2 electroreduction of about 0.3 V.

Our studies confirm that the EBH mixture lowers the overpotential for CO_2 reduction by shifting the CO_2/CO_2^- equilibrium potential positively, although the catalytic effect is not due to the formation of EMIM-CO_2 complexes and might instead be connected to a stabilization through hydrogen bonding of the CO_2^- radical inside a water cage in a water-in-salt environment. Improved catalysis by stabilization of unstable radicals in a suitable cage might be a general feature in catalysis, as suggested by recent reports involving aldehyde reduction[57] and reports of anti-Arrhenius kinetics in the electroreduction and electrooxidation, respectively, of CO_2 and CH_4 in gas hydrates at sub-zero temperatures.[58] Our results are also consistent with very recent

reports on the relevance of electrostatic stabilization of the CO_2^- radical for the electrochemical reduction of CO_2.[2,59–61]

This is also the first time that equilibrium potentials in non-aqueous solution have been calculated in the actual chemical environment and directly compared with experiments to reveal eventual catalytic effects of the solvent excluding effects from other components. Because the computational methods used herein can be applied to any redox couple in any solution, this can be a new protocol for studying homogeneous catalysis. The calculated equilibrium potentials can then be referred to practical reference scales, such as cAgCl or Fc^+/Fc, which can greatly enhance the synergy between computation and experiment and lead to improved understanding of electrocatalytic reactions, especially in non-aqueous solutions.[62–68]

AUTHOR INFORMATION

Corresponding Author

Jun Cheng - *State Key Laboratory of Physical Chemistry of Solid Surfaces, iChEM, College of Chemistry and Chemical Engineering, Xiamen University, Xiamen 361005, China; Innovation Laboratory for Sciences and Technologies of Energy Materials of Fujian Province (IKKEM), Xiamen, China;*

Email: chengjun@xmu.edu.cn

Angel Cuesta - *Department of Chemistry, School of Natural and Computing Sciences, University of Aberdeen, AB24 3UE, Scotland, UK; Centre for Energy Transition, University of Aberdeen, AB24 3FX, Scotland, UK;*

Email: angel.cuestaciscar@abdn.ac.uk

ASSOCIATED CONTENT

The following files are available free of charge.

Method of the potential shift V_0 correction, computational data of all equilibrium potentials calculations in both EBH mixture and pure water, atom labelling of EMIM-BF_4, RDF results in EBH mixture and validation of Fc^+/Fc vs cAgCl in EBH mixture. (PDF)

ACKNOWLEDGMENT

We are grateful for funding support from the National Natural Science Foundation of China (Grants Nos 21861132015, 21991151, 21991150, 22021001, 91745103, 92161113, 91945301 and 3502Z20203027). The support of the Leverhulme Trust (RPG-2015-0400) is gratefully acknowledged. We are also very grateful to the reviewers for their helpful suggestions to improve readability.

REFERENCES

(1) Yin, Z.; Peng, H.; Wei, X.; Zhou, H.; Gong, J.; Huai, M.; Xiao, L.; Wang, G.; Lu, J.; Zhuang, L. An Alkaline Polymer Electrolyte CO_2 Electrolyzer Operated with Pure Water. *Energ. Environ. Sci.* **2019**, *12* (8), 2455–2462. https://doi.org/10.1039/c9ee01204d.

(2) Bhargava, S. S.; Proietto, F.; Azmoodeh, D.; Cofell, E. R.; Henckel, D. A.; Verma, S.; Brooks, C. J.; Gewirth, A. A.; Kenis, P. J. A. System Design Rules for Intensifying the Electrochemical Reduction of CO_2 to CO on Ag Nanoparticles. *Chemelectrochem* **2020**, *7* (9), 2001–2011. https://doi.org/10.1002/celc.202000089.

(3) Edwards, J. P.; Xu, Y.; Gabardo, C. M.; Dinh, C.-T.; Li, J.; Qi, Z.; Ozden, A.; Sargent, E. H.; Sinton, D. Efficient Electrocatalytic Conversion of Carbon Dioxide in a Low-Resistance Pressurized Alkaline Electrolyzer. *Appl. Energ.* **2020**, *261*, 114305. https://doi.org/10.1016/j.apenergy.2019.114305.

(4) Endrődi, B.; Kecsenovity, E.; Samu, A.; Halmágyi, T.; Rojas-Carbonell, S.; Wang, L.; Yan, Y.; Janáky, C. High Carbonate Ion Conductance of a Robust PiperION Membrane Allows Industrial Current Density and Conversion in a Zero-Gap Carbon Dioxide Electrolyzer Cell. *Energ Environ. Sci.* **2020**, *13* (11), 4098–4105. https://doi.org/10.1039/d0ee02589e.

(5) Arquer, F. P. G. de; Dinh, C.-T.; Ozden, A.; Wicks, J.; McCallum, C.; Kirmani, A. R.; Nam, D.-H.; Gabardo, C.; Seifitokaldani, A.; Wang, X.; et al. CO_2 Electrolysis to Multicarbon Products at Activities Greater than 1 A cm^{-2}. *Science* **2020**, *367* (6478), 661–666. https://doi.org/10.1126/science.aay4217.

(6) Ma, W.; Xie, S.; Liu, T.; Fan, Q.; Ye, J.; Sun, F.; Jiang, Z.; Zhang, Q.; Cheng, J.; Wang, Y. Electrocatalytic Reduction of CO2 to Ethylene and Ethanol through Hydrogen-Assisted C–C Coupling over Fluorine-Modified Copper. *Nat. Catal.* **2020**, *3* (6), 478–487. https://doi.org/10.1038/s41929-020-0450-0.

(7) Weber, R. S. Effective Use of Renewable Electricity for Making Renewable Fuels and Chemicals. *ACS Catal.* **2019**, *9* (2), 946–950. https://doi.org/10.1021/acscatal.8b04143.

(8) Hori, Y.; Koga, O.; Yamazaki, H.; Matsuo, T. Infrared Spectroscopy of Adsorbed CO and Intermediate Species in Electrochemical Reduction of CO_2 to Hydrocarbons on a Cu Electrode. *Electrochim. Acta* **1995**, *40* (16), 2617–2622. https://doi.org/10.1016/0013-4686(95)00239-b.

(9) Hori, Y. Modern Aspects of Electrochemistry; Modern Aspects of Electrochemistry; Springer New York, 2008; Vol. 42, pp 89–189. https://doi.org/10.1007/978-0-387-49489-0_3.

(10) Rosen, B. A.; Salehi-Khojin, A.; Thorson, M. R.; Zhu, W.; Whipple, D. T.; Kenis, P. J. A.; Masel, R. I. Ionic Liquid–Mediated Selective Conversion of CO_2 to CO at Low Overpotentials. *Science* **2011**, *334* (6056), 643–644. https://doi.org/10.1126/science.1209786.

(11) Papasizza, M.; Yang, X.; Cheng, J.; Cuesta, A. Electrocatalytic Reduction of CO_2 in Neat and Water-Containing Imidazolium-Based Ionic Liquids. *Curr. Opin. Electrochem.* **2020**, *23*, 80–88. https://doi.org/10.1016/j.coelec.2020.04.004.

(12) Kutz, R. B.; Chen, Q.; Yang, H.; Sajjad, S. D.; Liu, Z.; Masel, I. R. Sustainion Imidazolium-Functionalized Polymers for Carbon Dioxide Electrolysis. *Energy Technol.* **2017**, *5* (6), 929–936. https://doi.org/10.1002/ente.201600636.

(13) Lau, G. P. S.; Schreier, M.; Vasilyev, D.; Scopelliti, R.; Grätzel, M.; Dyson, P. J. New Insights Into the Role of Imidazolium-Based Promoters for the Electroreduction of CO_2 on a Silver Electrode. *J. Am. Chem. Soc.* **2016**, *138* (25), 7820–7823. https://doi.org/10.1021/jacs.6b03366.

(14) Papasizza, M.; Cuesta, A. In Situ Monitoring Using ATR-SEIRAS of the Electrocatalytic Reduction of CO_2 on Au in an Ionic Liquid/Water Mixture. *ACS Catal.* **2018**, *8* (7), 6345–6352.https://doi.org/10.1021/acscatal.8b00977.

(15) Lim, H.-K.; Kwon, Y.; Kim, H. S.; Jeon, J.; Kim, Y.-H.; Lim, J.-A.; Kim, B.-S.; Choi, J.; Kim, H. Insight into the Microenvironments of the Metal–Ionic Liquid Interface during Electrochemical CO_2 Reduction. *ACS Catal.* **2018**, *8* (3), 2420–2427. https://doi.org/10.1021/acscatal.7b03777.

(16) Rosen, B. A.; Haan, J. L.; Mukherjee, P.; Braunschweig, B.; Zhu, W.; Salehi-Khojin, A.; Dlott, D. D.; Masel, R. I. In Situ Spectroscopic Examination of a Low Overpotential Pathway for Carbon Dioxide Conversion to Carbon Monoxide. *J. Phys. Chem. C* **2012**, *116* (29), 15307–15312. https://doi.org/10.1021/jp210542v.

(17) Rosen, B. A.; Zhu, W.; Kaul, G.; Salehi-Khojin, A.; Masel, R. I. Water Enhancement of CO_2 Conversion on Silver in 1-Ethyl-3-Methylimidazolium Tetrafluoroborate. *J. Electrochem. Soc.* **2013**, *160* (2), H138–H141. https://doi.org/10.1149/2.004303jes.

(18) Sun, L.; Ramesha, G. K.; Kamat, P. V.; Brennecke, J. F. Switching the Reaction Course of Electrochemical CO_2 Reduction with Ionic Liquids. *Langmuir* **2014**, *30* (21), 6302–6308. https://doi.org/10.1021/la5009076.

(19) Wang, Y.; Hatakeyama, M.; Ogata, K.; Wakabayashi, M.; Jin, F.; Nakamura, S. Activation of CO_2 by Ionic Liquid EMIM–BF_4 in the Electrochemical System: A Theoretical Study. *Phys. Chem. Chem. Phys.* **2015**, *17* (36), 23521–23531. https://doi.org/10.1039/c5cp02008e.

(20) Urushihara, M.; Chan, K.; Shi, C.; Nørskov, J. K. Theoretical Study of $EMIM^+$ Adsorption on Silver Electrode Surfaces. *J. Phys. Chem. C* **2015**, *119* (34), 20023–20029. https://doi.org/10.1021/acs.jpcc.5b07268.

(21) Braunschweig, B.; Mukherjee, P.; Haan, J. L.; Dlott, D. D. Vibrational Sum-Frequency Generation Study of the CO_2 Electrochemical Reduction at Pt/EMIM-BF_4 Solid/Liquid

Interfaces. *J. Electroanal. Chem.* **2017**, *800*, 144–150. https://doi.org/10.1016/j.jelechem.2016.10.035.

(22) Rey, N. G.; Dlott, D. D. Effects of Water on Low-Overpotential CO_2 Reduction in Ionic Liquid Studied by Sum-Frequency Generation Spectroscopy. *Phys. Chem. Chem. Phys.* **2017**, *19* (16), 10491–10501. https://doi.org/10.1039/c7cp00118e.

(23) Liu, S.; Tao, H.; Liu, Q.; Xu, Z.; Liu, Q.; Luo, J.-L. Rational Design of Silver Sulfide Nanowires for Efficient CO_2 Electroreduction in Ionic Liquid. *ACS Catal.* **2018**, *8* (2), 1469–1475. https://doi.org/10.1021/acscatal.7b03619.

(24) Kemna, A.; Rey, N. G.; Braunschweig, B. Mechanistic Insights on CO_2 Reduction Reactions at Platinum/[BMIM][BF_4] Interfaces from In Operando Spectroscopy. *ACS Catal.* **2019**, *9* (7), 6284–6292. https://doi.org/10.1021/acscatal.9b01033.

(25) Aylmer-Kelly, A. W. B.; Bewick, A.; Cantrill, P. R.; Tuxford, A. M. Studies of Electrochemically Generated Reaction Intermediates Using Modulated Specular Reflectance Spectroscopy. *Faraday Discuss. Chem. Soc.* **1973**, *56* (0), 96–107. https://doi.org/10.1039/dc9735600096.

(26) Chandrasekaran, K.; Bockris, L. O. In-Situ Spectroscopic Investigation of Adsorbed Intermediate Radicals in Electrochemical Reactions: CO_2^- on Platinum. *Surf. Sci.* **1987**, *185* (3), 495–514. https://doi.org/10.1016/s0039-6028(87)80173-5.

(27) Schwarz, H. A.; Dodson, R. W. Reduction Potentials of CO_2^- and the Alcohol Radicals. *J. Phys. Chem.* **1989**, *93* (1), 409–414. https://doi.org/10.1021/j100338a079.

(28) Surdhar, P. S.; Mezyk, S. P.; Armstrong, D. A. Reduction Potential of the Carboxyl Radical Anion in Aqueous Solutions. *J. Phys. Chem.* **1989**, *93* (8), 3360–3363. https://doi.org/10.1021/j100345a094.

(29) Amatore, C.; Saveant, J. M. Mechanism and Kinetic Characteristics of the Electrochemical Reduction of Carbon Dioxide in Media of Low Proton Availability. *J. Am. Chem. Soc.* **1981**, *103* (17), 5021–5023. https://doi.org/10.1021/ja00407a008.

(30) Cheng, J.; Liu, X.; VandeVondele, J.; Sulpizi, M.; Sprik, M. Redox Potentials and Acidity Constants from Density Functional Theory Based Molecular Dynamics. *Accounts Chem. Res.* **2014**, *47* (12), 3522–3529. https://doi.org/10.1021/ar500268y.

(31) Zeng, X.; Hu, H.; Hu, X.; Yang, W. Calculating Solution Redox Free Energies with Ab Initio Quantum Mechanical/Molecular Mechanical Minimum Free Energy Path Method. *J. Chem. Phys.* **2009**, *130* (16), 164111. https://doi.org/10.1063/1.3120605.

(32) Nørskov, J. K.; Rossmeisl, J.; Logadottir, A.; Lindqvist, L.; Kitchin, J. R.; Bligaard, T.; Jónsson, H. Origin of the Overpotential for Oxygen Reduction at a Fuel-Cell Cathode. *J. Phys. Chem. B* **2004**, *108* (46), 17886–17892. https://doi.org/10.1021/jp047349j.

(33) Keith, J. A.; Carter, E. A. Theoretical Insights into Pyridinium-Based Photoelectrocatalytic Reduction of CO_2. *J. Am. Chem. Soc.* **2012**, *134* (18), 7580–7583. https://doi.org/10.1021/ja300128e.

(34) Xu, S.; Carter, E. A. Theoretical Insights into Heterogeneous (Photo)Electrochemical CO_2 Reduction. *Chem. Rev.* **2019**, *119* (11), 6631–6669. https://doi.org/10.1021/acs.chemrev.8b00481.

(35) Bryantsev, V. S.; Diallo, M. S.; III, W. A. G. Calculation of Solvation Free Energies of Charged Solutes Using Mixed Cluster/Continuum Models. *J. Phys. Chem. B* **2008**, *112* (32), 9709–9719. https://doi.org/10.1021/jp802665d.

(36) Yang, X.-H.; Cuesta, A.; Cheng, J. The Energetics of Electron and Proton Transfer to CO_2 in Aqueous Solution. *Phys. Chem. Chem. Phys.* **2021**, *23* (38), 22035–22044. https://doi.org/10.1039/d1cp02824c.

(37) Tomasi, J.; Mennucci, B.; Cammi, R. Quantum Mechanical Continuum Solvation Models. *Chem. Rev.* **2005**, *105* (8), 2999–3094. https://doi.org/10.1021/cr9904009.

(38) Klamt, A.; Schüürmann, G. COSMO: A New Approach to Dielectric Screening in Solvents with Explicit Expressions for the Screening Energy and Its Gradient. *J. Chem. Soc. Perkin Transactions 2* **1993**, *0* (5), 799–805. https://doi.org/10.1039/p29930000799.

(39) Friedrichs, M.; Zhou, R.; Edinger, S. R.; Friesner, R. A. Poisson−Boltzmann Analytical Gradients for Molecular Modeling Calculations. *J. Phys. Chem. B* **1999**, *103* (16), 3057–3061. https://doi.org/10.1021/jp982513m.

(40) Andreussi, O.; Dabo, I.; Marzari, N. Revised Self-Consistent Continuum Solvation in Electronic-Structure Calculations. *J. Chem. Phys.* **2012**, *136* (6), 064102. https://doi.org/10.1063/1.3676407.

(41) Dupont, C.; Andreussi, O.; Marzari, N. Self-Consistent Continuum Solvation (SCCS): The Case of Charged Systems. *J. Chem. Phys.* **2013**, *139* (21), 214110. https://doi.org/10.1063/1.4832475.

(42) Fisicaro, G.; Genovese, L.; Andreussi, O.; Marzari, N.; Goedecker, S. A Generalized Poisson and Poisson-Boltzmann Solver for Electrostatic Environments. *J. Chem. Phys.* **2016**, *144* (1), 014103. https://doi.org/10.1063/1.4939125.

(43) Nishihara, S.; Otani, M. Hybrid Solvation Models for Bulk, Interface, and Membrane: Reference Interaction Site Methods Coupled with Density Functional Theory. *Phys. Rev. B* **2017**, *96* (11), 115429. https://doi.org/10.1103/physrevb.96.115429.

(44) Cheng, J.; Sulpizi, M.; Sprik, M. Redox Potentials and pKa for Benzoquinone from Density Functional Theory Based Molecular Dynamics. *J. Chem. Phys.* **2009**, *131* (15), 154504. https://doi.org/10.1063/1.3250438.

(45) Yang, X.-H.; Cuesta, A.; Cheng, J. Computational Ag/AgCl Reference Electrode from Density Functional Theory-Based Molecular Dynamics. *J. Phys. Chem. B* **2019**, *123* (48), 10224–10232. https://doi.org/10.1021/acs.jpcb.9b06650.

(46) Pavlishchuk, V. V.; Addison, A. W. Conversion Constants for Redox Potentials Measured versus Different Reference Electrodes in Acetonitrile Solutions at 25°C. *Inorg. Chim. Acta* **2000**, *298* (1), 97–102. https://doi.org/10.1016/s0020-1693(99)00407-7.

(47) Cheng, J.; VandeVondele, J. Calculation of Electrochemical Energy Levels in Water Using the Random Phase Approximation and a Double Hybrid Functional. *Phys. Rev. Lett.* **2016**, *116* (8), 086402. https://doi.org/10.1103/physrevlett.116.086402.

(48) VandeVondele, J.; Krack, M.; Mohamed, F.; Parrinello, M.; Chassaing, T.; Hutter, J. Quickstep: Fast and Accurate Density Functional Calculations Using a Mixed Gaussian and Plane Waves Approach. *Comput. Phys. Commun.* **2005**, *167* (2), 103–128. https://doi.org/10.1016/j.cpc.2004.12.014.

(49) Becke, A. D. Density-Functional Exchange-Energy Approximation with Correct Asymptotic Behavior. *Phys. Rev. A* **1988**, *38* (6), 3098–3100. https://doi.org/10.1103/physreva.38.3098.

(50) Lee, C.; Yang, W.; Parr, R. G. Development of the Colle-Salvetti Correlation-Energy Formula into a Functional of the Electron Density. *Phys. Rev. B* **1988**, *37* (2), 785–789. https://doi.org/10.1103/physrevb.37.785.

(51) Goedecker, S.; Teter, M.; Hutter, J. Separable Dual-Space Gaussian Pseudopotentials. *Phys. Rev. B* **1995**, *54* (3), 1703–1710. https://doi.org/10.1103/physrevb.54.1703.

(52) Hartwigsen, C.; Goedecker, S.; Hutter, J. Relativistic Separable Dual-Space Gaussian Pseudopotentials from H to Rn. *Phys. Rev. B* **1998**, *58* (7), 3641–3662. https://doi.org/10.1103/physrevb.58.3641.

(53) Grimme, S. Semiempirical GGA-type Density Functional Constructed with a Long-range Dispersion Correction. *J. Comput. Chem.* **2006**, *27* (15), 1787–1799. https://doi.org/10.1002/jcc.20495.

(54) Kühne, T. D. Second Generation Car–Parrinello Molecular Dynamics. *Wiley Interdiscip. Rev.: Comput. Mol. Sci.* **2014**, *4* (4), 391–406. https://doi.org/10.1002/wcms.1176.

(55) Lan, J.; Hutter, J.; Iannuzzi, M. First-Principles Simulations of an Aqueous CO/Pt(111) Interface. *J. Phys. Chem. C* **2018**, *122* (42), 24068–24076. https://doi.org/10.1021/acs.jpcc.8b05933.

(56) *CRC Handbook of Chemistry and Physics, 86th Edition Edited by David R. Lide (National Institute of Standards and Technology). CRC Press (an Imprint of Taylor and Francis Group): Boca Raton, FL. 2005. 2544 Pp. $125.96. ISBN 0-8493-0486-5.*; Lide, D. R., Ed.; Journal of the American Chemical Society; 2006; Vol. 128. https://doi.org/10.1021/ja059868l.

(57) Paul, A.; Shipman, M. A.; Onabule, D. Y.; Sproules, S.; Symes, M. D. Selective Aldehyde Reductions in Neutral Water Catalysed by Encapsulation in a Supramolecular Cage. *Chem. Sci.* **2021**, *12* (14), 5082–5090. https://doi.org/10.1039/d1sc00896j.

(58) Sargeant, E.; Kolodziej, A.; Duff, C. S. L.; Rodriguez, P. Electrochemical Conversion of CO_2 and CH_4 at Subzero Temperatures. *ACS Catal.* **2020**, *10* (14), 7464–7474. https://doi.org/10.1021/acscatal.0c01676.

(59) Monteiro, M. C. O.; Dattila, F.; Hagedoorn, B.; García-Muelas, R.; López, N.; Koper, M. T. M. Absence of CO_2 Electroreduction on Copper, Gold and Silver Electrodes without Metal

Cations in Solution. *Nat. Catal.* **2021**, *4* (8), 654–662. https://doi.org/10.1038/s41929-021-00655-5.

(60) Bhargava, S. S.; Cofell, E. R.; Chumble, P.; Azmoodeh, D.; Someshwar, S.; Kenis, P. J. A. Exploring Multivalent Cations-Based Electrolytes for CO_2 Electroreduction. *Electrochim. Acta* **2021**, *394*, 139055. https://doi.org/10.1016/j.electacta.2021.139055.

(61) Resasco, J.; Chen, L. D.; Clark, E.; Tsai, C.; Hahn, C.; Jaramillo, T. F.; Chan, K.; Bell, A. T. Promoter Effects of Alkali Metal Cations on the Electrochemical Reduction of Carbon Dioxide. *J. Am. Chem. Soc.* **2017**, *139* (32), 11277–11287. https://doi.org/10.1021/jacs.7b06765.

(62) Alam, M. T.; Masud, J.; Islam, Md. M.; Okajima, T.; Ohsaka, T. Differential Capacitance at Au(111) in 1-Alkyl-3-Methylimidazolium Tetrafluoroborate Based Room-Temperature Ionic Liquids. *J. Phys. Chem. C* **2011**, *115* (40), 19797–19804. https://doi.org/10.1021/jp205800x.

(63) Gnahm, M.; Müller, C.; Répánszki, R.; Pajkossy, T.; Kolb, D. M. The Interface between Au(100) and 1-Butyl-3-Methyl-Imidazolium - Hexafluorophosphate. *Phys. Chem. Chem. Phys.* **2011**, *13* (24), 11627–11633. https://doi.org/10.1039/c1cp20562e.

(64) Müller, C.; Vesztergom, S.; Pajkossy, T.; Jacob, T. The Interface between Au(100) and 1-Butyl-3-Methyl-Imidazolium-Bis(Trifluoromethylsulfonyl)Imide. *J. Electroanal. Chem.* **2015**, *737*, 218–225. https://doi.org/10.1016/j.jelechem.2014.06.010.

(65) Corsetti, F.; Mostofi, A. A. System-Size Convergence of Point Defect Properties: The Case of the Silicon Vacancy. *Phys. Rev. B* **2011**, *84* (3), 035209. https://doi.org/10.1103/physrevb.84.035209.

(66) Siinor, L.; Lust, K.; Lust, E. Electrical Double Layer Capacitance at Bi(111)|1-Ethyl-3-Methylimidazolium Tetrafluoroborate Interface as a Function of the Electrode Potential. *J. Electrochem. Soc.* **2010**, *157* (7), F83. https://doi.org/10.1149/1.3430106.

(67) Oll, O.; Romann, T.; Pikma, P.; Lust, E. Spectroscopy Study of Ionic Liquid Restructuring at Lead Interface. *J. Electroanal. Chem.* **2016**, *778*, 41–48. https://doi.org/10.1016/j.jelechem.2016.08.016.

(68) Kruusma, J.; Tõnisoo, A.; Pärna, R.; Nõmmiste, E.; Lust, E. In Situ X-Ray Photoelectron Spectroscopic and Electrochemical Studies of the Bromide Anions Dissolved in 1-Ethyl-3-

Methyl Imidazolium Tetrafluoroborate. *Nanomaterials* **2019**, *9* (2), 304. https://doi.org/10.3390/nano9020304.

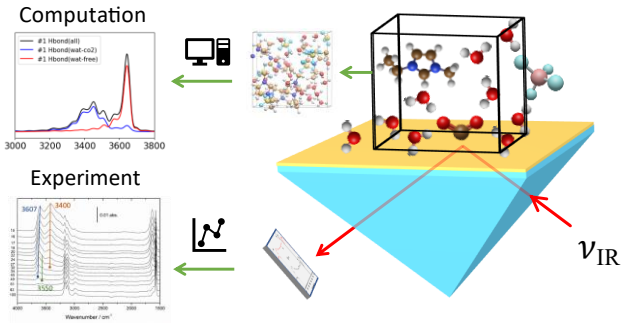

For Table of Contents Only

(Supporting information)

Water-in-salt environment reduces the overpotential for reduction of CO_2 to CO_2^- in ionic liquid/water mixtures

Xiao-Hui Yang[a], Marco Papasizza[b,†], Angel Cuesta[b,c,] and Jun Cheng[a,d,*]*

[a] *State Key Laboratory of Physical Chemistry of Solid Surfaces, iChEM, College of Chemistry and Chemical Engineering, Xiamen University, Xiamen 361005, China.*

[b] *Department of Chemistry, School of Natural and Computing Sciences, University of Aberdeen, AB24 3UE, Scotland, UK.*

[c] *Centre for Energy Transition, University of Aberdeen, AB24 3FX, Scotland, UK.*

[d] *Innovation Laboratory for Sciences and Technologies of Energy Materials of Fujian Province (IKKEM), Xiamen, China.*

† Current address: Sweetch Energy, 6 Rue Pierre Joseph Colin, 3500 Rennes, France.

KEYWORDS: electrochemical reduction of CO_2, room temperature ionic liquid, *ab initio* molecular dynamics, absorption infrared spectra, hydrogen bond networks

S1. Computational methods

S1.1 Thermodynamic integration.

The free energy changes for the electron transfer or particle solvation reactions are calculated with a combination of the free energy perturbation (FEP) theory and the thermodynamic integration (TI) method. In FEP theory, two states can be connected by a linear combination through a coupling parameter, η ($\eta \in [0,1]$). Thus, a thermodynamic path (η from 0 to 1) between two states is constructed, where the two ends of the path ($\eta = 0$ and 1) correspond to the initial and final states, respectively. Thus, a fictitious hybrid energy state can be written as

$$E_\eta = (1-\eta)E_0 + \eta E_1, \tag{S1}$$

where E_0 and E_1 are the potential energy of the initial and final states, respectively. The free energy change (ΔA) is obtained exactly using the TI method,

$$\Delta A = \int_0^1 d\eta \langle \Delta E \rangle_\eta, \tag{S2}$$

where $\langle \Delta E \rangle_\eta$ is the ensemble average of the energy difference between the reactant and product states at a fixed configuration (*i.e.*, vertical energy gap $\Delta E = \frac{\partial E_\eta}{\partial \eta} = E_1 - E_0$).[1]

S1.2 Free energy calculations.

We use a generic redox couple X^-/X to represent the computation of electron-transfer free energies. Using the TI method in eq. S2, the free energy of oxidation (reduction) from X^- to X (X to X^-) can be obtained by reversibly removing (inserting) an electron from the AIMD simulation under periodic boundary conditions (PBC). However, directly inserting an electron in a PBC system charges the system, and renders the reference for the electrostatic potential uncertain. This electrostatic potential uncertainty is due to the standard Ewald summation under PBC. The electrostatic potential of the charged system has a potential shift $V_{0,X^-/X}$ compared to the neutral system, and thus the oxidation free energy $\Delta A_{X^-/X}$ obtained from eq. S2 does not correspond to the adiabatic ionization free energy (AIP_{X^-}), by a difference equal to $q_{X^-/X} \cdot V_{0,X^-/X}$.[2] The AIP_{X^-} can therefore be obtained from eq. S3, where $q_{X^-/X} = -1$ is the total charge difference between the initial and final states.[3]

$$AIP_{X^-} = \Delta A_{X^-/X} - q_{X^-/X} \cdot V_{0,X^-/X} \tag{S3}$$

S1.3 Computational Ag/AgCl ($a_{Cl^-} = 1$) reference electrode (cAgCl).

A computational Ag/AgCl reference electrode is developed to recover the potential reference under PBC.[4] For a specific oxidation reaction X^-/X with respect to the cAgCl, its full reaction and the corresponding equilibrium potential ($U_{X^-/X}^{Ag/AgCl}$) are

$$X^-(aq) + AgCl(s) \longrightarrow X(aq) + Cl^-(aq) + Ag(s) \tag{S4a}$$

$$U_{\mathrm{X^-/X}}^{\mathrm{Ag/AgCl}} = \Delta \mathrm{G}/e_0. \quad \text{(S4b)}$$

The overall reaction in eq. S4a is composed of two half-reactions, the anodic reaction and the cathodic reaction. The anodic reaction is the oxidation of the solvated species X^- to X, thus the electrode reaction and the corresponding absolute equilibrium potential of X^-/X ($U_{\mathrm{X^-/X}}^{\mathrm{abs}}$) are

$$\mathrm{X^-(aq)} \longrightarrow \mathrm{X(aq)} + \mathrm{e^-(vac.)}, \quad \text{(S5a)}$$

$$U_{\mathrm{X^-/X}}^{\mathrm{abs}} = \mathrm{AIP_{X^-}}/e_0. \quad \text{(S5b)}$$

Where the $\mathrm{AIP_{X^-}}$ is considered as the electronic work function of an electron bound in solvated X^-, and is obtained from the computation by using the TI method (eq. S3). The cathodic reaction and the corresponding absolute electrode potential ($U_{\mathrm{Ag/AgCl}}^{\mathrm{abs}}$) are

$$\mathrm{AgCl(s)} + e^-(vac.) \longrightarrow \mathrm{Cl^-(aq)} + \mathrm{Ag(s)}, \quad \text{(S6a)}$$

$$U_{\mathrm{Ag/AgCl}}^{\mathrm{abs}} = (\Delta_{\mathrm{f}} G_{\mathrm{Cl^-}}^{\mathrm{g,o}} - W_{\mathrm{Cl^-}})/e_0. \quad \text{(S6b)}$$

Where $\Delta_{\mathrm{f}} G_{\mathrm{Cl^-}}^{\mathrm{g,o}} = -1.3\mathrm{eV}$ is the standard Gibbs free energy of formation of the gas phase chloride anion, and $W_{\mathrm{Cl^-}}$ is the work function of Cl^-.

This $W_{\mathrm{Cl^-}}$ is the energy of extracting a solvated Cl^- from the electrolyte to the gas phase, and can be obtained from computation by using the TI method, *i.e.*, a chloride ion is reversibly inserted and removed. In practice, the Cl^- is not directly removed but replaced by a dummy, in order to preserve the location for the subsequent insertion of the Cl^-. The dummy should have zero interactions with electrolytes. However, if no restraints are applied on the dummy, it could overlap with solvent molecules, and thus the subsequent insertion of the Cl^- cannot have a logical configuration. To avoid the overlap between inserted Cl^- and solvent molecules, we apply a repulsive potential between the dummy and solvent molecules. Same as the above-described calculation of oxidation free energy in eq. S3, reversibly inserting and removing the chloride ion in the system under PBC also lead to a potential shift ($V_{0,\mathrm{Cl^-}}$) in the charged system compared to the natural system. Therefore, the desolvation free energy ($\Delta A_{\mathrm{Cl^-}}$) obtained from eq. S2 also has a corresponding potential shift ($q_{\mathrm{Cl^-}} \cdot V_{0,\mathrm{Cl^-}}$), and $q_{\mathrm{Cl^-}} = -1$ is the total charge difference between the initial and final states. In addition, due to the repulsive potential applied to the dummy, a cavity is formed around the dummy. The formation energy of this cavity (ΔA_{LJ}) is then obtained by using the TI method in eq. S2.[4] Please note that the work function of Cl^- corresponds to transferring it from the electrolyte to the gas phase, not to removing it altogether. Therefore, the total energy of Cl^- in the gas phase ($\Delta E_{\mathrm{Cl^-}}$) needs to be added back. In summary, the equation to calculate the work function is

$$W_{\mathrm{Cl^-}} = \Delta A_{\mathrm{Cl^-}} - \Delta A_{\mathrm{LJ}} + \Delta E_{\mathrm{Cl^-}} - q_{\mathrm{Cl^-}} \cdot V_{0,\mathrm{Cl^-}}. \quad \text{(S7)}$$

After substituting the $W_{\mathrm{Cl^-}}$ in eq. S6b and the $\mathrm{AIP_{X^-}}$ in eq. S5b by eqs. S7 and S3, respectively, the equation to calculate the equilibrium potential of X^-/X with respect to the cAgCl is

$$e_0 U_{X^-/X}^{Ag/AgCl} = AIP_{X^-} + \Delta_f G_{Cl^-}^{g,o} - W_{Cl^-}$$
$$= \Delta A_{X^-/X} + \Delta_f G_{Cl^-}^{g,o} - \Delta A_{Cl^-} + \Delta A_{LJ} - \Delta E_{Cl^-} + (q_{Cl^-} \cdot V_{0,Cl^-} - q_{X^-/X} \cdot V_{0,X^-/X}) \quad \text{(S8)}$$

If the $\Delta A_{X^-/X}$ and ΔA_{Cl^-} are obtained in the same computational setup (*e.g.*, unit-cell dimensions, number of solvent molecules, and density functional approximations), the corresponding potential shift $q_{X^-/X} \cdot V_{0,X^-/X}$ and $q_{Cl^-} \cdot V_{0,Cl^-}$ are the same.[4] In this case, the last term $(q_{Cl^-} \cdot V_{0,Cl^-} - q_{X^-/X} \cdot V_{0,X^-/X})$ in eq. S8 is zero, and thus the resulting equation for the equilibrium potential calculation of X^-/X with respect to the cAgCl is

$$e_0 U_{X^-/X}^{Ag/AgCl} = \Delta A_{X^-/X} + \Delta_f G_{Cl^-}^{g,o} - \Delta A_{Cl^-} + \Delta A_{LJ} - \Delta E_{Cl^-}. \quad \text{(S9)}$$

S1.4 Correction of potential shift V_0

The potential shift $q \cdot V_0$ in eq. S8 is a correction term with respect to vacuum. It can be cancelled if the same computational setup is used in simulation. Alternatively, this potential correction term can also be interpreted by employing the electrostatic potential of bulk solvent ε. Taking the calculation of $\Delta A_{X^-/X}$ as an example, the corresponding potential shift is $q_{X^-/X} \cdot V_{0,X^-/X}$. If a constant C can be employed as the potential difference between vacuum and the potential in this unit-cell where the solvent electrostatic potential is zero ($\varepsilon^0 = 0$), the potential correction can be replaced by

$$q_{X^-/X} \cdot V_{0,X^-/X} = q_{X^-/X}(C + (\varepsilon_{X^-} - \varepsilon^0)) \quad \text{(S10)}$$

Where the ε_{X^-} represents the electrostatic potential of bulk solvent when the simulation net charge is not zero. Similarly, in the calculation of ΔA_{Cl^-}, the potential correction can be replaced by

$$q_{Cl^-} \cdot V_{0,Cl^-} = q_{Cl^-}(C + (\varepsilon_{Cl^-} - \varepsilon^0)) \quad \text{(S11)}$$

Therefore, the last term $(q_{Cl^-} \cdot V_{0,Cl^-} - q_{X^-/X} \cdot V_{0,X^-/X})$ in eq. S8 is

$$q_{Cl^-} \cdot V_{0,Cl^-} - q_{X^-/X} \cdot V_{0,X^-/X} = q_{Cl^-} \cdot \varepsilon_{Cl^-} - q_{X^-/X} \cdot \varepsilon_{X^-}. \quad \text{(S12)}$$

Where $q_{X^-/X} = -1$ and $q_{Cl^-} = -1$ are the total charge difference between the initial and final states. Substituting the above eq. S12 into eq. S8, and the equilibrium potential of X^-/X redox couple against the Ag/AgCl ($a_{Cl^-} = 1$) reference electrode is:

$$e_0 U_{X^-/X}^{Ag/AgCl} = \Delta A_{X^-/X} + \Delta_f G_{Cl^-}^{g,o} - \Delta A_{Cl^-} + \Delta A_{LJ} - \Delta E_{Cl^-} + \left(q_{Cl^-} \cdot \varepsilon_{Cl^-} - q_{X^-/X} \cdot \varepsilon_{X^-}\right)$$
$$= \Delta A_{X^-/X} - \Delta A_{Cl^-} + \Delta A_{LJ} - E_{Cl^-} + \Delta_f G_{Cl^-}^{g,o} + e_0(\varepsilon_{X^-} - \varepsilon_{Cl^-}) \quad \text{(S13)}$$

S2. Fc/Fc^+ gas phase ionization energies

To evaluate the energy difference derived by DFT approximations in equilibrium potential calculations, the ionization energy (IP) of Fc/Fc^+ in the gas phase were calculated and validated with well accepted experimental results. Table S1 shows ionization energies of Fc/Fc^+ with different basis sets and functionals, basis sets like double-ζ basis with polarization function (DZVP-MOLOPT-SR-GTH), triple-ζ basis with two sets of polarization functions (TZP2P- MOLOPT-SR-GTH) and quadruple-ζ basis with polarization function (Ahlrichs-def2-QZVP) were employed. Core electrons were also represented by the Goedecker-Teter-Hutter (GTH) pseudopotentials in calculations with a notation "Yes", while the calculation with "all electrons" means no pseudopotential is employed in the calculation. Here, the 2s, 2p electrons of C, the 3s, 3p, 3d, 4s electrons of Fe were treated as valence electrons.

Table S1. Calculated ionization potentials of Fc/Fc^+ in the gas phase. ΔE is the difference with the experimental value. The experimental value is adopted from the NIST Chemistry WebBook.[5]

Functionals / basis sets / pseudopotentials	Total energy (Hartree)		IP (eV)	$\Delta E_{Fc/Fc^+}$ (eV)
	Fc	Fc+		
BLYP / DZVP / Yes	-185.924	-185.690	6.373	-0.337
BLYP / TZV2P / Yes	-185.938	-185.700	6.457	-0.253
HSE06 / DZVP / Yes	-186.197	-185.964	6.336	-0.374
HSE06 / TZV2P / Yes	-186.206	-185.971	6.397	-0.313
B3LYP / TZV2P / Yes	-186.038	-185.812	6.147	-0.563
BLYP / QZVP / all_electrons	-1650.924	-1650.680	6.637	-0.073
Exp.			6.71	

According to the results in Table S1, ionization energies can be properly calculated at GGA level with large basis set employed without pseudopotentials. Due to the limitation of computational cost, our DFTMD simulations were performed with pseudopotentials and the basis set is DZVP. Therefore, the ionization energy difference $\Delta E_{Fc/Fc^+}$ was directly added in eq. S13, and the final equation to calculate the Fc/Fc^+ equilibrium potential was replaced by:

$$e_0 U_{Fc/Fc^+}^{Ag/AgCl} = \Delta A_{Fc/Fc^+} - \Delta E_{Fc/Fc^+} - \Delta A_{Cl^-} + \Delta A_{LJ} - E_{Cl^-} + \Delta_f G_{Cl^-}^{g,o} + e_0(\varepsilon_{X^-} - \varepsilon_{Cl^-}) \quad (S14)$$

S3. Modelling setup

Table S2. Computational setup of the three models in this work.

Computational setup				
Models	**Box size L (Å)**	**Electrolytes**	**Basis sets**	**Pseudopotentials**
CO_2/CO_2^-	13.39	6 EMIM-BF_4 and 26 water molecules	TZV2P-GTH	1s electrons of B, C, N, O F
Fc/Fc^+	13.80	6 EMIM-BF_4 and 26 water molecules	DZVP-GTH	1s electrons of B, C, N, O, F; 1s, 2s, and 2p electrons of Fe
Cl^- solvation	13.39	6 EMIM-BF_4 and 26 water molecules	TZV2P-GTH	1s electrons of B, C, N, O, F; 1s, 2s and 2p electrons of Cl

Table S3. Parameters used in Langevin dynamics during the SGCPMD.

Parameters for Langevin dynamics				
Models	**Gamma (fs^{-1})**	**Noisy gamma of each thermo region**		
		EMIM-BF_4	**Water**	**Solute**
CO_2/CO_2^-	1.00E-03	2.00E-04	2.20E-04	2.20E-04
Fc/Fc^+	1.00E-03	2.00E-04	2.20E-04	2.00E-04
Cl^- solvation	1.00E-03	2.00E-04	2.20E-04	2.20E-04

S4. Fc/Fc^+ equilibrium potential in aqueous solution

The Fc/Fc^+ equilibrium potential with respect to the computational Ag/AgCl ($a_{Cl^-} = 1$ M) reference electrode was calculated by employing Equation S5. Free energies such as $\Delta A_{Fc/Fc^+}$, ΔA_{Cl^-} and ΔA_{LJ} are obtained by employing the thermodynamic integration approach. Here energies related to the work function of Cl^-, W_{Cl^-}, was adopted from previous work, and the setup inconsistency was corrected by recalculating free energy differences. Thus, the only term that needs to be calculated is the oxidation free energy of Fc/Fc^+.

S4.1 Computational details. The simulation box for Fc/Fc^+ was cubic cell with size at L = 12.80 Å, including 62 water molecules and 1 Fc/Fc^+ solute. Canonical (NVT) ensemble underwent Langevin molecular dynamics in this work and the temperature of the system was 300 K. Time step of this simulation was 0.5 fs and the cut-off energy of the finest grid level of plane wave density was set to 400 Ry. The SGCPMD simulation was performed with the BLYP functional for the exchange correlation approximation, double-ζ basis with polarization functions (DZVP-MOLOPT-SR-GTH)

standard basis set, Goedecker-Teter-Hutter (GTH) pseudopotentials and the van der Waals correction with Grimme D3 method. The production periods of DFTMD simulations are ~6 ps after more than 2 ps equilibration.

S4.2 Fc/Fc^+ vs. cAgCl in aqueous solution. The molecular dynamic simulation of Fc/Fc^+ in aqueous solution was carried out for about 6 ps, and the energy convergence was shown in the Figure S1 below.

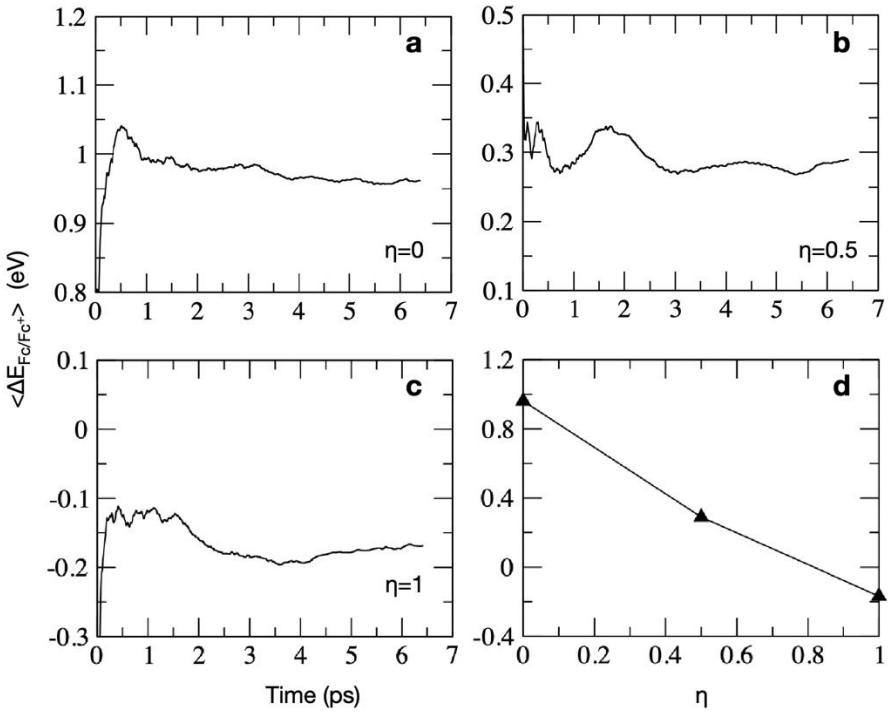

Figure S1. Time accumulation averages of the vertical energies (a, b and c) and thermodynamic integration path (d) for Fc/Fc^+ redox couple oxidation reaction in aqueous solution. Three integration points ($\eta = 0, 0.5, 1$) are presented in (a, b and c), respectively. The picture (d) is the averaged vertical energy difference $\langle \Delta E \rangle_\eta$ as a function of the coupling parameter η.

The free energy of ΔA_{Cl^-} in previous work is obtained with the basis set TZV2P, and the value is about 0.43 eV compare to the DZVP basis set. Therefore, the ΔA_{Cl^-} is 407.54 eV in this work and the formation energy of cavity in the simulation is the same as in the previous work $\Delta A_{LJ} = 0.21$ eV. Electrostatic potentials of both ε_{Fc^+} and ε_{Cl^-} were cumulatively averaged from the edges of the simulation box. Once the total energy of gas phase chloride $E_{Cl^-} = -407.45$ eV is obtained to yield the potential of Fc/Fc^+ vs. Ag/AgCl in aqueous solution (Table S4).

Table S4. Summary of free energies used in Equation S5 and the equilibrium potential of Fc/Fc^+ vs. Ag/AgCl ($a_{Cl^-} = 1$ M) in water. $eU_{Fc\backslash Fc^+}^{Ag/AgCl}$ is the calculated equilibrium potential while eU_{exp} is the result in experiment. Error of this calculation is ΔU_{error}=0.1 eV.

$\Delta A_{Fc\backslash Fc^+}$	ε_{Fc^+}	ΔA_{Cl^-}	ε_{Cl^-}	ΔA_{LJ}	$eU_{Fc\backslash Fc^+}^{Ag/AgCl}$	eU_{exp}	ΔU_{error}
0.33	0.69	407.54	-0.11	0.21	0.28	0.18	0.10

S5. Chemical structure of EMIM-BF_4.

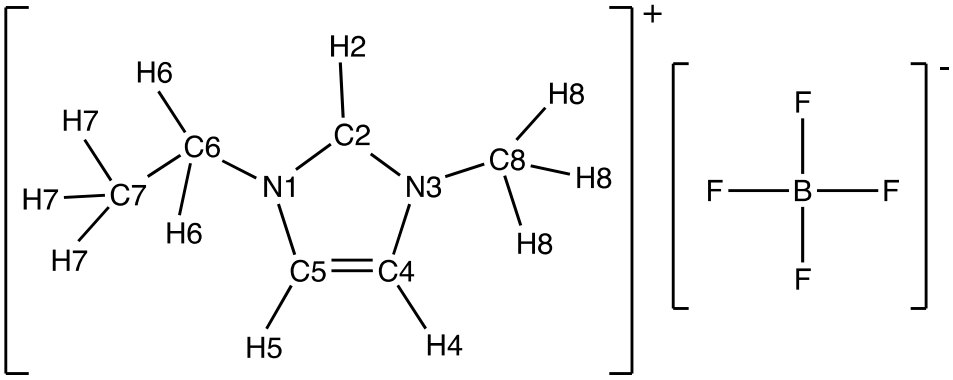

Figure S2. Atom labelling used in this work. The $EMIM^+$ is the cation on the left, and BF_4^- is the anion on the right hand.

S6. Free energy calculations in the EBH mixture.

The equilibrium potentials of Fc/Fc^+ and CO_2^-/CO_2 with respect to cAgCl in the EBH mixture were calculated by employing Equations S5 and S4, respectively. Helmholtz free energies ΔA were obtained by employing the TI approach, which requires the averaged vertical energy gap $\langle \Delta E \rangle_\eta$.

S6.1. Calculation of $\Delta A_{CO_2^-/CO_2}$. The oxidation free energy of CO_2^-/CO_2 redox couple, $\Delta A_{CO_2^-/CO_2}$, was firstly calculated at GGA level with BLYP functional and TZV2P basis sets, then $\Delta A_{CO_2^-/CO_2}$ at HSE06 level with the same basis set was obtained by recalculating the vertical energy difference. Table S5 below shows all calculated vertical energies for the oxidation free energy of CO_2^-/CO_2.

Table S5. Summary of vertical energy gap $\langle \Delta E \rangle_\eta$ and the corresponding thermodynamic integrations $\Delta A_{CO_2^-/CO_2}$ calculated in this work.

CO_2^-/CO_2 with TZV2P basis set		
η	BLYP	HSE06
0	0.60	1.29
0.25	-2.47	-2.51
0.5	-2.59	-2.63
1	-2.79	-2.83
$\Delta A_{CO_2^-/CO_2}$	-2.21	-2.16

S6.2. Calculation of ΔA_{Cl^-}. The solvation free energy of Cl^- in the mixture solvent, ΔA_{Cl^-}, was firstly calculated at GGA level with BLYP functional and TZV2P basis sets, then ΔA_{Cl^-} at different functionals and different basis sets were also obtained by recalculating the vertical energy difference. Table S6 below shows all energies corresponding to the calculation of Cl^- work function.

Table S6. Summary of vertical energy gap $\langle \Delta E \rangle_\eta$ and the corresponding thermodynamic integrations ΔA_{Cl^-} calculated in this work. Total energies of Cl^- in the gas phase were also included.

Cl^-/dummy with	TZV2P basis set		DZVP basis set	
η	BLYP	HSE06	BLYP	HSE06
0	408.43	409.75	408.24	409.59
0.5	407.12	408.41	406.89	408.14
1	405.79	407.02	405.38	406.57
ΔA_{Cl^-}	407.14	408.43	406.89	408.14
E_{Cl^-}	-408.12	-409.29	-407.45	-408.64

S6.3. Calculation of $\Delta A_{Fc/Fc^+}$. The oxidation free energy of Fc/Fc^+ redox couple,$\Delta A_{Fc/Fc^+}$, was firstly calculated at GGA level with BLYP functional and DZVP basis sets, then $\Delta A_{Fc/Fc^+}$ at HSE06 level with the same basis set was obtained by recalculating the vertical energy difference. Table S7 below shows all calculated vertical energies for the oxidation free energy of CO_2^-/CO_2.

Table S7. Summary of vertical energy gap $\langle \Delta E \rangle_\eta$ and the corresponding thermodynamic integrations $\Delta A_{\mathrm{Fc/Fc^+}}$ calculated in this work.

Fc/Fc$^+$ with DZVP basis set		
η	BLYP	HSE06
0	0.28	0.24
0.5	-0.26	-0.29
1	-0.62	-0.65
$\Delta A_{\mathrm{Fc/Fc^+}}$	-0.23	-0.26

S6.4. Calculation of ΔA_{LJ}. The last one that requires thermodynamic integral calculation is the formation energy of the cavity ΔA_{LJ} in the electrolyte. This formation energy calculation was carried out in the classical molecular dynamics, and forcefields employed in this simulation were borrowed from Ghoshdastidar et al.'s work, and little difference were confirmed when employing OPLS/AA parameters. The derivative of the potential energy in this work was calculated by using the finite difference method. Here, the range of σ was changed from 0 to 3.5 Å, and averaged $\langle dE/d\sigma \rangle_\sigma$ at different integration points σ are presented in Figure S3, and the integration value is $\Delta A_{\mathrm{LJ}} = 0.14$ eV.

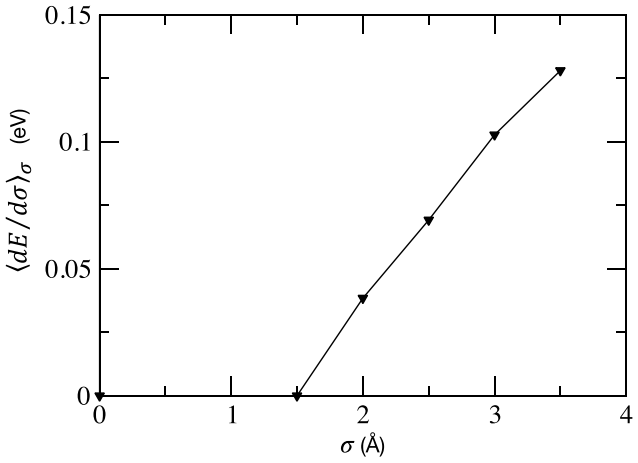

Figure S3. The averaged derivative of the potential energy surface $\langle dE/d\sigma \rangle_\sigma$ as a function of the finite distance σ. Integration of the plot from σ = 0 to 3.5 Å yields the formation energy of the cavity, ΔA_{LJ}. Integration points σ smaller than 1.5 Å were ignored because the derivative result is less than 10^{-4} eV, thus the actual integration starts from 1.5 Å.

S7. Equilibrium potential results in EBH mixture.

Table S8. Equilibrium potentials of CO_2^-/CO_2 and Fc/Fc^+ redox couples in the 18mol% EBH mixtures with respect to cAgCl. $\Delta\varepsilon_{\mathrm{bulk}} = (\varepsilon_{\mathrm{X}^-} - \varepsilon_{\mathrm{Cl}^-})$ is the electrostatic potential difference between two simulations.

Energy	GGA/BLYP	Hybrid/HSE06
$\mathrm{CO_2^-/CO_2}$ vs. cAgCl		
$\Delta A_{\mathrm{Cl}^-/d}$	407.14	408.43
ΔA_{LJ}	0.14	0.14
E_{Cl^-}	-408.12	-409.29
$\Delta A_{\mathrm{CO_2^-/CO_2}}$	-2.21	-2.16
$\Delta\varepsilon_{\mathrm{bulk}}$	0.30	0.30
$eU^{\mathrm{Ag/AgCl}}_{\mathrm{CO_2^-/CO_2}}$	-2.10	-2.16
$\mathrm{Fc/Fc^+}$ vs. cAgCl		
$\Delta A_{\mathrm{Cl}^-/d}$	406.89	408.14
ΔA_{LJ}	0.14	0.14
E_{Cl^-}	-407.45	-408.64
$\Delta A_{\mathrm{Fc/Fc^+}}$	-0.23	-0.26
$\Delta \mathrm{E}_{\mathrm{Fc/Fc^+}}$	0.34	0.37
$\Delta\varepsilon_{\mathrm{bulk}}$	0.66	0.66
$eU^{\mathrm{Ag/AgCl}}_{\mathrm{Fc/Fc^+}}$	0.18	0.11

S8. Validation of Fc^+/Fc vs cAgCl in EBH mixture.

The computed Fc^+/Fc equilibrium potential with respect to the computational Ag/AgCl reference electrode in the 18 mol% EMIM-BF_4/water mixture is 0.2 V at the GGA level and 0.1 V using the hybrid functional HSE06. This is in good agreement with the experimental value of 0.156 ± 0.010 V reported by Ohsaka and co-workers,[6] measured with a homemade Ag/AgCl wire immersed in the pure (*i.e.*, dry and chloride-free) EMIM-BF_4. Because our computational Ag/AgCl reference electrode is calculated for activity of chloride 1, we have corrected Ohsaka's and co-workers' value assuming that, in their case, the activity of Cl^- is determined by the solubility product of AgCl, as follows:

$$U_{\mathrm{Au/sol}}^{\mathrm{Ag/AgCl,wire}} = U_{\mathrm{Au/sol}}^{\mathrm{Ag/AgCl}} - \frac{RT}{F}\ln a_{\mathrm{Cl^-}}$$
$$\approx U_{\mathrm{Au/sol}}^{\mathrm{Ag/AgCl}} - \frac{RT}{2F}\ln K_{\mathrm{sp}} \qquad \text{(S15)}$$

Where the K_{sp} is the solubility product of AgCl in the mixture, R is ideal gas constant, T is the temperature in Kelvin and F is the Faraday constant. Kakiuchi et al.[7] reported the solubility of AgCl in 1-Methyl-3-octylimidazolium bis(trifluoromethanesulfonyl)imide ([$OMIM^+$][$TFSA^-$], to be 6.3×10^{-5} mol L^{-1} at room temperature, about 5 times more soluble than in water. If the solubilities of AgCl in EMIM-BF_4 and OMIM-TFSA are assumed to be similar, the potential of Ohsaka's and co-workers' "homemade Ag/AgCl wire" with respect to our computational Ag/AgCl ($a_{\mathrm{Cl^-}} = 1$ M) reference electrode is about 0.25 V. An additional difference is that our simulations correspond to an 18 mol% EMIM-BF_4/water mixture as opposed to dry EMIM-BF_4. If we ignore this difference, the experimental Fc^+/Fc equilibrium potential of 0.156 V measured by Ohsaka and co-workers corresponds to -0.09 V in our computational Ag/AgCl ($a_{\mathrm{Cl^-}} = 1$ M) scale. The result of our simulation (0.1 V), is therefore about 0.2 V more positive.

Considering the various approximations involved in the computation, and errors to the approximate value of the K_{sp} difference between the two different mixtures, this is an acceptable error. To better illustrate the source of the 0.2 V error, here, we list the specific approximations as follows.

1. The solubility of AgCl in pure EMIM-BF_4 was not found. Thus, we use the solubility of AgCl in pure [$OMIM^+$][-$TFSA^-$]. In this step, we assume the solubility difference between two ionic liquids, EMIM-BF_4 and [$OMIM^+$][-$TFSA^-$], is small.
2. After having the solubility of AgCl in pure ionic liquid, we assume that the activity of Cl^- can be obtained from the solubility product in such a low concentration of Cl^-, as shown in Eq. S15.
3. In this way, we concluded that our result is about 0.2 V positive compared to the experiment. However, please note that the chemical potential difference between the 18 mol% EBH mixture and pure EMIM-BF_4 is not considered yet. The solubility of AgCl in the [$OMIM^+$][-$TFSA^-$] is about 5 times larger than water, and thus if the water content increases, this error is reduced.

4. We know that the experimentally measured Fc/Fc^+ is 0.4 V in water, while it is 0.625 V in EBH, and about 0.68 V in pure EMIM-BF_4. Therefore, not only the chemical potential of Cl^- is different in pure EMIM-BF_4 and EBH mixture, but also the equilibrium potential of Fc/Fc^+ changes if the water content increases.

In practical equilibrium potential calculations, none of the above assumptions are included, and thus the error should be much smaller than 0.2 V.

S9. References

(1) Cheng, J.; Sulpizi, M.; Sprik, M. Redox Potentials and pKa for Benzoquinone from Density Functional Theory Based Molecular Dynamics. *J Chem Phys* **2009**, *131* (15), 154504. https://doi.org/10.1063/1.3250438.

(2) Cheng, J.; Sprik, M. Alignment of Electronic Energy Levels at Electrochemical Interfaces. *Phys Chem Chem Phys* **2012**, *14* (32), 11245–11267. https://doi.org/10.1039/c2cp41652b.

(3) Cheng, J.; Liu, X.; VandeVondele, J.; Sulpizi, M.; Sprik, M. Redox Potentials and Acidity Constants from Density Functional Theory Based Molecular Dynamics. *Accounts Chem Res* **2014**, *47* (12), 3522–3529. https://doi.org/10.1021/ar500268y.

(4) Yang, X.-H.; Cuesta, A.; Cheng, J. Computational Ag/AgCl Reference Electrode from Density Functional Theory-Based Molecular Dynamics. *J Phys Chem B* **2019**, *123* (48), 10224–10232. https://doi.org/10.1021/acs.jpcb.9b06650.

(5) Lias, S. G., "Ionization Energy Evaluation" in NIST Chemistry WebBook, NIST Standard Reference Database Number 69, Eds. Linstrom, P.J. and Mallard, W.G., National Institute of Standards and Technology, Gaithersburg MD, 20899, https://doi.org/10.18434/T4D303, (retrieved January 1, 2021)

(6) Alam, M. T.; Islam, Md. M.; Okajima, T.; Ohsaka, T. Measurements of Differential Capacitance in Room Temperature Ionic Liquid at Mercury, Glassy Carbon and Gold Electrode Interfaces. *Electrochem Commun* **2007**, *9* (9), 2370–2374. https://doi.org/10.1016/j.elecom.2007.07.009.

(7) Kakiuchi, T.; Yoshimatsu, T.; Nishi, N. New Class of Ag/AgCl Electrodes Based on Hydrophobic Ionic Liquid Saturated with AgCl. *Anal Chem* **2007**, *79* (18), 7187–7191. https://doi.org/10.1021/ac070820v.